ACS NANO

www.acsnano.org

ARTICLE

In Situ Forming Epidermal Bioelectronics for Daily Monitoring and Comprehensive Exercise

Hao Tang, Yuanfang Li, Baiqi Chen, Xing Chen, Yulong Han, Ming Guo, Hong-qi Xia,* Rong Song, Xingcai Zhang,* and Jianhua Zhou*

Cite This: https://doi.org/10.1021/acsnano.2c03414

Read Online

ACCESS | Metrics & More | Article Recommendations | Supporting Information

ABSTRACT: **Conventional epidermal bioelectronics usually do not conform well with natural skin surfaces and are susceptible to motion artifact interference, due to incompatible dimensions, insufficient adhesion, imperfect compliance, and usually require complex manufacturing and high costs. We propose *in situ* forming hydrogel electrodes or electronics (ISF-HEs) that can establish highly conformal interfaces on curved biological surfaces without auxiliary adhesions. The ISF-HEs also have favorable flexibility and soft compliance comparable to human skin (≈0.02 kPa^{-1}), which can stably maintain synchronous movements with deformed skins. Thus, the as-prepared ISF-HEs can accurately monitor large and tiny human motions with short response time (≈180 ms), good biocompatibility, and excellent performance. The as-obtained nongapped hydrogel electrode-skin interfaces achieve ultralow interfacial impedance (≈50 KΩ), nearly an order of magnitude lower than commercial Ag|AgCl electrodes as well as other reported dry and wet electrodes, regardless of the intrinsic micro-obstacles (wrinkles, hair) and skin deformation interference. Therefore, the ISF-HEs can collect high-quality electrocardiography and surface electromyography (sEMG) signals, with high signal-to-noise ratio (SNR ≈ 32.04 dB), reduced signal crosstalk, and minimized motion artifact interference. Simultaneously monitoring human motions and sEMG signals have also been implemented for the general exercise status assessment, such as the shooting competition in the Olympics. The as-prepared ISF-HEs can be considered as supplements/substitutes of conventional electrodes in percutaneously noninvasive monitoring of multifunctional physiological signals for health and exercise status.**

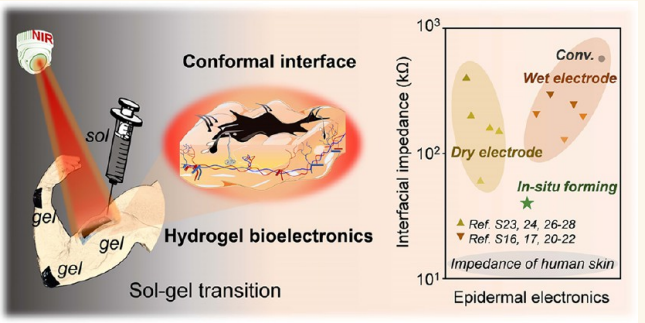

KEYWORDS: *in situ forming, epidermal bioelectronics, highly conformal interface, motion monitoring, electromyography recording*

Human skin, as the largest organ of the human body, is directly exposed to the external environment and provides a large number of significant physiological and biochemical signals closely associated with the human health status.[1−5] Effectively obtaining multifunctional physiological signals noninvasively through the skin is of great significance for daily health monitoring, clinical disease diagnosis, and treatment.[6−8] The past few decades have witnessed the rapid progress of epidermal bioelectronics.[9,10] Generally, the available wearable bioelectronics show an indispensable demand for the essential soft and flexible sensing interface, which will establish highly conformal interfaces on the highly wrinkled and stretchable skins to facilitate the collection and transmission of transdermal signals.[11−14] However, the current main difficulty is also the actual nonconformal contact between the relatively stiff epidermal bioelectronics and the soft biological surfaces,[15−17] which is likely to cause the undesirable attenuation or loss of crucial signals, even ultimately resulting in serious misunderstanding and misdiagnosis. In addition, the flexible interfaces with imperfect conformability are susceptible to motion artifacts, due to the relative interfacial sliding caused by the asynchronous motions with the skin deformation.[18,19] The main existing solution to overcome the above-mentioned challenges is applying the highly adhesive epidermal electronics on the irregular skin surface.[20−22]

The state-of-the-art wearable epidermal bioelectronics, whether self-adhesive or externally assisted, are mostly transferred and attached to the biological surface of interest.[23−26] Conventional adhesive electrodes can mainly

Received: April 7, 2022
Accepted: September 30, 2022

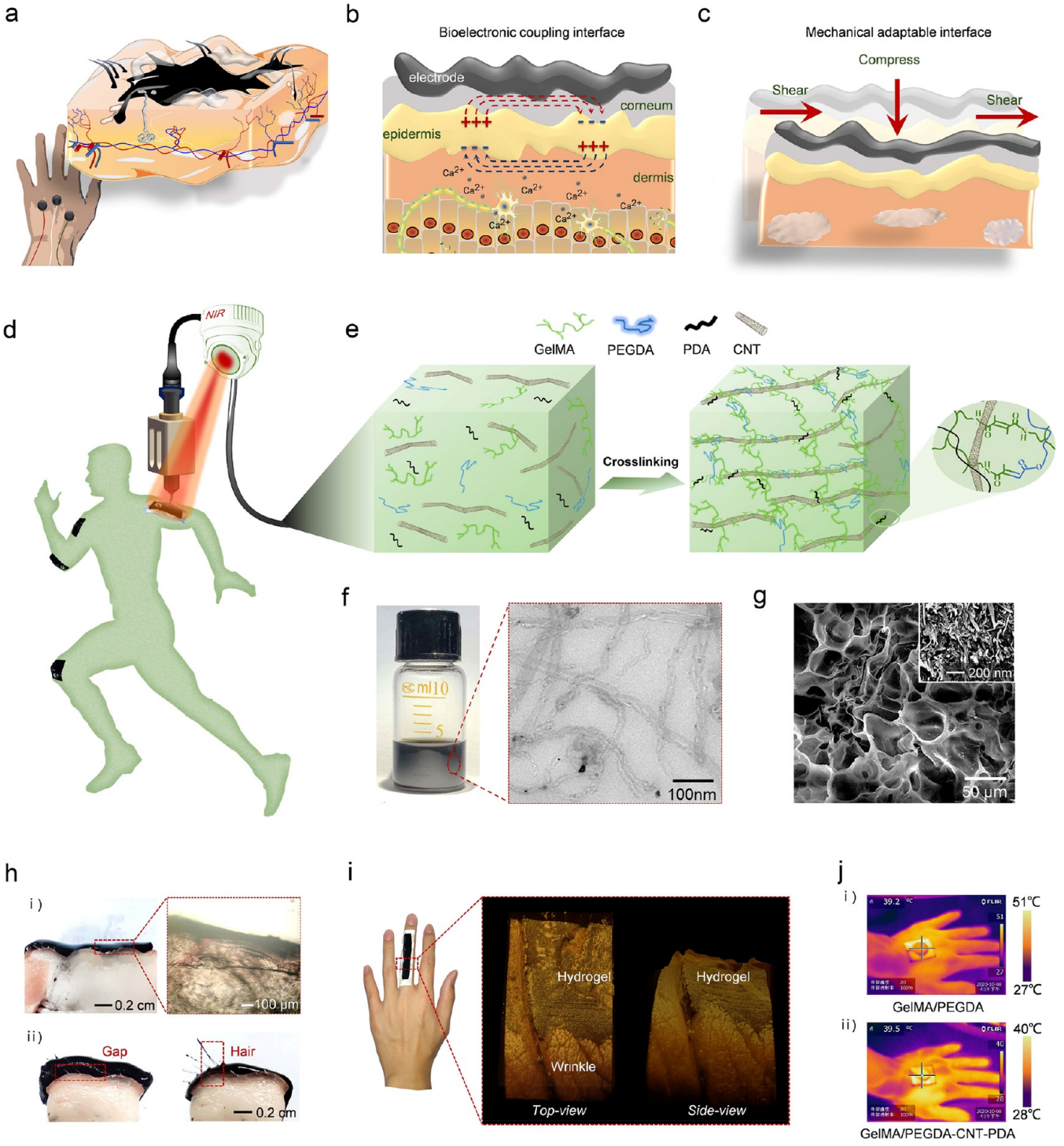

Figure 1. Design principle and facile preparation of ISF-HEs. (a) Schematic of the *in situ* forming epidermal electrode on the wrinkled skin that was covered with hair and soaked with sweat. (b) Schematic of the bioelectronic coupling interface established on the uneven biological surface. (c) Schematic of the mechanical adaptable interface on the biological surface subject to compression and shear stress. (d) Design strategy showing the *in situ* cross-linking of injectable hydrogels induced by NIR light to form highly conformal ISF-HEs on the surface of human skin. (e) Facile preparation and cross-linking process of GelMA/PEGDA-CNT-PDA composite conductive hydrogels. (f) Optical photo of the black composite precursor solution and its TEM image. (g) SEM image of the as-prepared GelMA/PEGDA-CNT-PDA hydrogel. The enlarged view showing CNTs embedded in hydrogel matrix. (h) Photos of the ISF-HE interfaces on pigskin model. No tiny gaps could be observed even under the microscope (i); the ordinary adhesive hydrogels were hindered by the hair structures (ii, left), while the *in situ* forming hydrogels successfully penetrated into the hair gaps (ii, right). (i) OCT images of the ISF-HE interfaces on human skin model. (j) Infrared camera photos of GelMA/PEGDA and GelMA/PEGDA-CNT-PDA hydrogels on the skin surface during their *in situ* cross-linking process.

establish macroscopically conformal interfaces on the complex biological surfaces, where there are still micron-level or even larger gaps due to the inherent obstructions such as micron-scale wrinkles and pores. Recent researches have demonstrated

https://doi.org/10.1021/acsnano.2c03414
ACS Nano XXXX, XXX, XXX−XXX

that the conformal and intimate contacts would largely depend on the intrinsic thickness of the epidermal electronics, which would primarily determine the overall stiffness of the interface material and the adhesive energy for the cohesive contact.[15,19] The relatively thinner flexible electronics even with the grid or zigzag microstructures, such as electronic tattoos with nanoscale thickness, would have better compliance and flexibility and be thus more likely to maintain perfect conformity with the skin microstructure.[27,28] Nevertheless, such thin epidermal bioelectronics with the thickness of submicron scale are extremely difficult to fabricate and manipulate, also arguing for high cost and cutting-edge techniques.[29,30]

With the development of flexible composite or hybrid electronic materials, the additive manufacturing and rapid processing of multifunctional flexible epidermal structures and electronics could ultimately be realized. Researchers have used direct ink writing to create patterned electronic tattoos on the skin. These liquid metal and silver paste-based electronic tattoos are highly conformal to the biological surface, but far inferior to bioactive composite conductive hydrogels in terms of interfacial elasticity, making it difficult to monitor epidermal deformation and motion signals.[13,14] Herein, we are working on designing and developing the *in situ* forming hydrogel epidermal bioelectronics, which can be directly obtained by the rapid and feasible cross-linking or curing of the precursor solutions under mild conditions, without other complicated fabrication techniques. The precursor solutions will penetrate the tiny gaps of micro-obstacles such as wrinkles and hair due to the intrinsic fluidity, achieving thorough and close contact with the essential skin. The *in situ* forming conformal interfaces would maximize the favorable contact areas between the epidermal electronics and the wrinkled skins, which will minimize the signal transmission impedance and effectively facilitate percutaneously monitoring health information. What's more, the *in situ* forming hydrogel electronics with appropriate softness and elasticity compatible with human soft, irregular tissues tend to establish the mechanical environment-adaptable interfaces. In this case, the flexible interfaces can maintain stable and synchronous movements with the curved skins in the long term, greatly avoiding the motion artifact interference caused by skin deformations.[20]

Based on the design principle proposed above, a highly conformal hydrogel bioelectronic interface was formed *in situ* on the wrinkled skin surface, through the near-infrared (NIR) light gently and feasibly initiating the rapid thermal cross-linking of the hydrogel precursor aqueous solutions. The as-prepared composite electronic materials of methacrylate gelatin/poly(ethylene-glycol) diacrylate, carbon nanotube, and polydopamine (GelMA/PEGDA-CNT-PDA) hydrogel components would possess the ideal conductivity, adjustable mechanical and bioadhesive properties as well as excellent biocompatibility. The *in situ* forming hydrogel electrodes or electronics (ISF-HEs) would maintain superior conformity with the wrinkled skins, regardless of the hydrogel interface thicknesses and the skin deformations. Therefore, the as-prepared epidermal hydrogel strain sensors based on the ISF-HEs could accurately monitor the large-scale as well as tiny human motions with relatively high sensitivity (gauge factor (GF) of 1.23), rapid response (<200 ms), and long-term durability (>500 cycles). The highly conformal hydrogel electrode−skin interface would exhibit an ultralow interfacial impedance, nearly an order of magnitude lower than those of the ordinary adhesive hydrogel electrodes (AHEs) based on the prefabricated composite hydrogels, and the commercial Ag|AgCl electrodes (CEs). Besides, the ISF-HEs could also collect high-quality surface electromyography (sEMG) signals in real-time, with the increased signal-to-noise ratio (SNR) level, minimized signal crosstalk, and antimotion artifact or skin deformation interference. Furthermore, simultaneously monitoring human motions and sEMG signals during exercise have also been successfully arranged, for the effective assessment of the typical shooting process of athletes and subsequent guidance training.

RESULTS AND DISCUSSION

Design Principle and Preparation of ISF-HEs on Skin.

The flexible sensing interface or epidermal electrode, as an essential component of human wearable electronics, is in close contact with the skin directly and noninvasively monitors or obtains multifunctional physiological and biochemical signal from the skin.[4,8] In order to highly accurately and quite efficiently acquire and transmit the signal of interest percutaneously, the ideal epidermal electrode is required to be able to adapt to local mechanical environment changes caused by motion and tolerate wet environment erosion caused by sweating as well as overcome the inherent hair, wrinkles, and other microstructure obstacles on the skin, to maintain excellent and stable compliance with the curved skin, while remaining a relatively low interfacial contact impedance (Figure 1a). Therefore, the *in situ* forming electrode, which can penetrate into the hair and wrinkle gaps and maintain the closest contact with the biological tissues in the flowing state before curing, will become the best substitute for the conventional adhesive electrode (Figure S1). The *in situ* forming electrode can establish a nearly nongapped interface on the biological surface, immensely reducing the interfacial contact impedance and increasing the bioelectronic coupling process of electron and ion transferring between the interfaces (Figure 1b), which is greatly beneficial for high-quality bioelectric signal acquisition.

Currently, hydrogel bioelectronics have been becoming a hot spot for the advancement of wearable devices.[8,23] And multifunctional hydrogel substrate materials, directly cross-linked from precursor aqueous solutions with favorable fluidity, have created the possibility of ISF-HEs. In this case, bioactive hydrogels are cross-linked *in situ* under mild conditions after being transferred or injected onto the desired biological surface, during which hydrogel biomacromolecules with terminal active groups are likely to interact intimately with biological tissues, thus forming firmly self-adhesive, flexible and elastic interfaces.[22] Now that bioactive hydrogels possess the most compatible mechanical characteristics for biological tissues (such as elastic modulus), the as-prepared ISF-HEs can be reasonably conformal to the wrinkled biological surface, even when they undergo tensile or compressive deformations caused by the dynamic muscle activity (Figure S2). As a consequence, this mechanical environment-adaptable and self-adhesive hydrogel epidermal electrode deforms synchronously with the biological surface in motion, avoiding unwanted fine gaps at the electrode-tissue interfaces. Briefly, the as-prepared ISF-HEs are expected to establish a highly conformal electrode-tissue interface, greatly reducing the contact impedance toward the inherent impedance of biological surfaces as well as minimizing the impact of local stress

https://doi.org/10.1021/acsnano.2c03414
ACS Nano XXXX, XXX, XXX−XXX

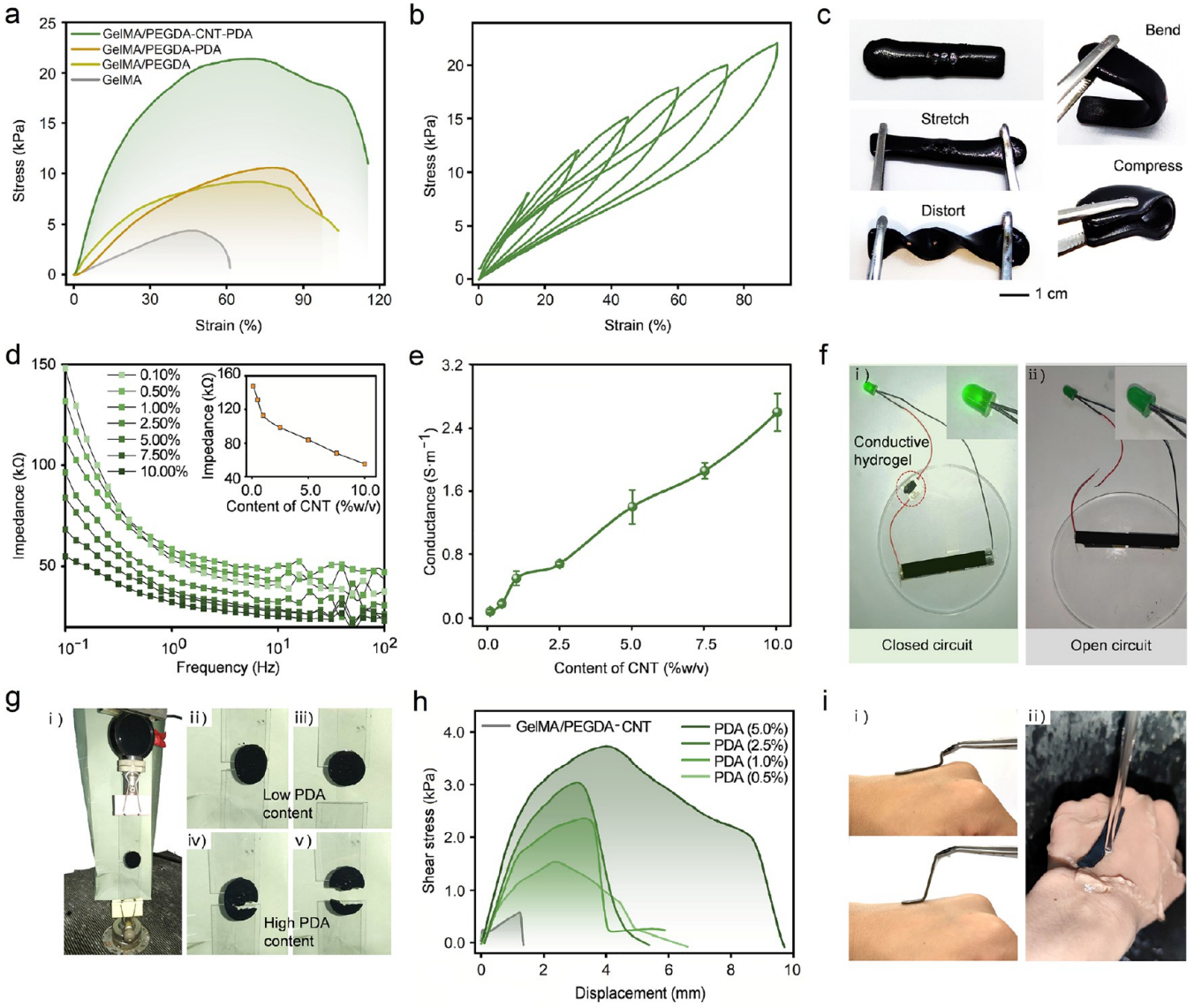

Figure 2. Mechanical properties, electrical conductivity and bioadhesion of ISF-HEs. (a) Tensile stress−strain curves of composite hydrogels with different components. (b) Stress−strain curves of GelMA/PEGDA-CNT-PDA hydrogels under step loading−unloading tests. (c) Photos of the composite hydrogels before and after being stretched, twisted, bent and compressed. (d) Electrochemical impedance spectra of composite hydrogels. The inset showing the impedance values of the hydrogels at 0.1 Hz. (e) Changes in the conductance (σ) of composite conductive hydrogels. (f) Photos of the luminous LED using the composite hydrogel as a conductor (i), and the extinguished LED in the open circuit (ii). (g) Overall adhesion performance test process of the composite hydrogel (i), and pictures of the hydrogels with low PDA content of 0.5 wt%: adhesion (ii), falling off (iii), as well as the hydrogels with high PDA content of 5 wt%: beginning to break (iv) and complete break (v). (h) Displacement-shear stress curves of composite hydrogels. (i) Photos of the as-prepared ISF-HEs being peeled off from the human skin (i), and the composite hydrogels with resistance to the flushing of running water (ii).

environment changes (e.g., motion artifacts) on the stable interfaces (Figure 1c).

Therefore, a kind of available and practical epidermal electrode materials, the GelMA/PEGDA-CNT-PDA composite conductive hydrogels, were prepared by NIR induced one-step thermal cross-linking of the premixed precursor aqueous solutions containing different proportions of GelMA, PEGDA, hydrophilic CNTs, and dopamine (DA) prepolymer solution (Figure 1d,e, Figure S3). In this way, a black conductive ink was facilely prepared by ultrasonic mixing uniformly in advance. Transmission electron microscopy (TEM) image clearly shows that CNTs were homogeneously and stably dispersed in the water phase, indicating that the hydrophilic CNTs were well entangled with other polymer chains through hydrogen bonds and other intermolecular forces (Figure 1f). Under infrared radiation, the C═C double bonds on the methacrylamide groups of GelMA molecular chains and the end of PEGDA chains underwent a NIR induced free radical cross-linking to form a three-dimensional hydrogel network. In the highly microporous freeze-dried conductive hydrogel structure (Figure 1g), there was no obvious CNT agglomerations in the pore wall areas formed by the accumulation of polymer chains, indicating that almost all CNTs were well embedded in the polymer network (Figure S4).

Generally, GelMA or PEGDA hydrogels were prepared by ultraviolet (UV) light-induced radical polymerization in most literature, while this approach was not feasible here since the addition of CNTs to the precursor solutions greatly reduced

https://doi.org/10.1021/acsnano.2c03414
ACS Nano XXXX, XXX, XXX−XXX

the permeability of UV light after all (Figure S7). Therefore, after introducing the common low-temperature redox initiation system ($K_2S_2O_8$/$NaHSO_3$), NIR light with stronger penetration ability and photothermal conversion effect was applied to induce thermal free radical cross-linking of conductive ink. Under the irradiation of infrared physiotherapy lamps (Figure S8), conductive ink could be used to write "BME", "SYSU" characters directly on paper or draw delicate patterns on flexible PDMS substrate and on the skin surface. And the fine patterns of the hydrogel would remain stable on the wrinkled skin, which further proved the possibility of NIR induced *in situ* formation of hydrogels. Different from the ordinary hydrogels that were applied to the tissue after preforming, the *in situ* forming hydrogels could smoothly penetrate into the hair gap of the pig skin in a fluid state (Figure 1h) and be more closely combined with the microstructure such as the folds on the tissue surface under microscope observation. Figure 1i shows photos of a large area of conductive ink forming hydrogels *in situ* on the finger with the foam tape mold. After removing the tape mold, the complete composite hydrogels with different thicknesses of 1000 μm, 500 μm, or 100 μm remained on the skin covered with hair, and the hydrogels could also be removed without residue (Figure S9). Furthermore, optical coherence tomography (OCT) images clearly exhibit that the *in situ* forming hydrogels maintained close contact with almost all the skin structures as a whole, regardless of the skin wrinkles and hair gaps (Figure 1i, Figure S10). Besides, the infrared camera photos display the whole temperature distributions of the human skin during the gelation of composite conductive ink (40 °C) and pure GelMA/PEGDA precursor solutions (51 °C) (Figure 1j). The addition of CNTs and PDA components with favorable photothermal conversion effects could distinctly shorten the NIR radiation time and thus reduce the overall environment temperature, which also proved that there was basically no risk of burns during the *in situ* forming of composite conductive hydrogels.

Mechanical Properties, Electrical Conductivity, and Bioadhesion of ISF-HEs. To ensure the ISF-HEs function normally and stably on the biological surface, relatively superior electrical activity and appropriate biomechanical properties matching the biological tissue are urgently in demand. Here, the mechanical properties of composite hydrogels were first improved by introducing PEGDA and CNTs into the pure GelMA hydrogel network. PEGDA provided more cross-linking sites to increase the cross-linking density of the hydrogel network, while inorganic CNT fibers were entangled well with polymer molecular chains to resist deformation. Figure S11a–c shows the compressive and tensile stress–strain curves of GelMA/PEGDA-CNT-PDA composite hydrogels with different PEGDA ratios and CNT content, respectively. The Young's modulus of the composite hydrogels increased to 72.54 kPa with the CNT content of 10% w/v (Figure S11d). Overall, the mechanical properties of composite conductive hydrogels were significantly improved compared to the pure GelMA hydrogels (Figure 2a, Table S1). It is worth mentioning that, the as-prepared composite hydrogels will be comparable to human skin (with the elastic modulus of 60–850 kPa) and other biological tissues in terms of elastic modulus.[31] Furthermore, as shown in Figure 2b, the composite hydrogels would exhibit a moderate range of reversible stretchability, with the negligible residual strain under loading–unloading tests. In addition, after undergoing multiple cyclic tensile tests, the dissipative energy of the composite hydrogels gradually stabilized at a lower level, demonstrating their durable antifatigue performance (Figure S11f). More intuitively, unlike GelMA hydrogels that were prone to break under external forces (Figure S12), the as-prepared reinforced composite hydrogels could remain undeformed and unbroken even after being slightly stretched, twisted, bent, and compressed (Figure 2c).

The electric conductivity of the composite conductive hydrogel would come from the incorporated CNTs. Figure 2d shows the electrochemical impedance spectra (EIS) of conductive hydrogels with different CNT content, and the inset displays that the impedance value of the conductive hydrogel at 0.1 Hz decreased significantly as the CNT content increased. The cyclic voltammetry (CV) also demonstrated that the charge storage capacity of the conductive hydrogel gradually increased with the increasing CNT content. Additionally, there were no obvious cathodic peak and anodic peak in the CV curves, suggesting no redox process and the electrochemical stability of the conductive hydrogels (Figure S13). Both EIS and CV results indicated that as the filling density of CNT increased, the resistance of charge carriers transferring in different regions decreased, causing the overall conductivity of the hydrogels to increase. The conductance (σ) of the composite conductive hydrogels was also measured and calculated systematically. As shown in Figure 2e, the conductance gradually increased with the increasing CNT content and reached 2.63 $S{\cdot}m^{-1}$ at CNT content of 10% w/v. Moreover, the conductance of the corresponding dehydrated hydrogels eventually reached 92 $S{\cdot}m^{-1}$ due to the large amount of water loss, the shrinkage of the hydrogels, and the increasing density of CNT packing in the porous hydrogel (Figure S13). The electrical conductivity of the composite hydrogels was further visually demonstrated by acting as a conductor in a closed circuit to light up a light-emitting diode (LED) (Figure 2f).

In order to enhance the bioadhesive properties of the ISF-HE composite materials, PDA prepolymers with a large number of catechol structures on the molecular chain were introduced into the hydrogel network. The adhesive strength of the as-prepared GelMA/PEGDA-CNT-PDA hydrogels with different PDA ratios was evaluated by operating their tensile adhesion experiments. Intuitively, the composite hydrogels were first adhered to two clean glass slides, which were then slowly pulled by the universal material testing machine at a constant speed (Figure 2g(i)). Hydrogels with lower adhesion would eventually fall off the glass after slow pulling (Figure 2g(ii,iii)), while hydrogels with higher adhesion would break into two pieces after slow pulling but still adhere to the glass slides (Figure 2g(iv,v). Figure 2h clearly demonstrates that the shear stress strength gradually increased with the increasing content of PDA and achieved a maximum adhesive strength of 3.94 kPa (5.0 wt% PDA to glass). The composite hydrogels also showed favorable adhesion to metals, plastics and paper (Figure S14), and the ISF-HEs could still adhere firmly to the skin surface during the peeling process (Figure 2i(i)). The excellent tissue adhesion performance was mainly ascribed to the superior interfacial binding affinity between these abundant catechol groups of the hydrogel network and nucleophiles ($-NH_2$ and $-SH$ groups of lysine and cysteine, respectively) widely existing on the surface of biological tissues. Therefore, the as-prepared ISF-HE composite materials likewise exhibited superior wet tissue adhesion performance and still adhered to

https://doi.org/10.1021/acsnano.2c03414
ACS Nano XXXX, XXX, XXX–XXX

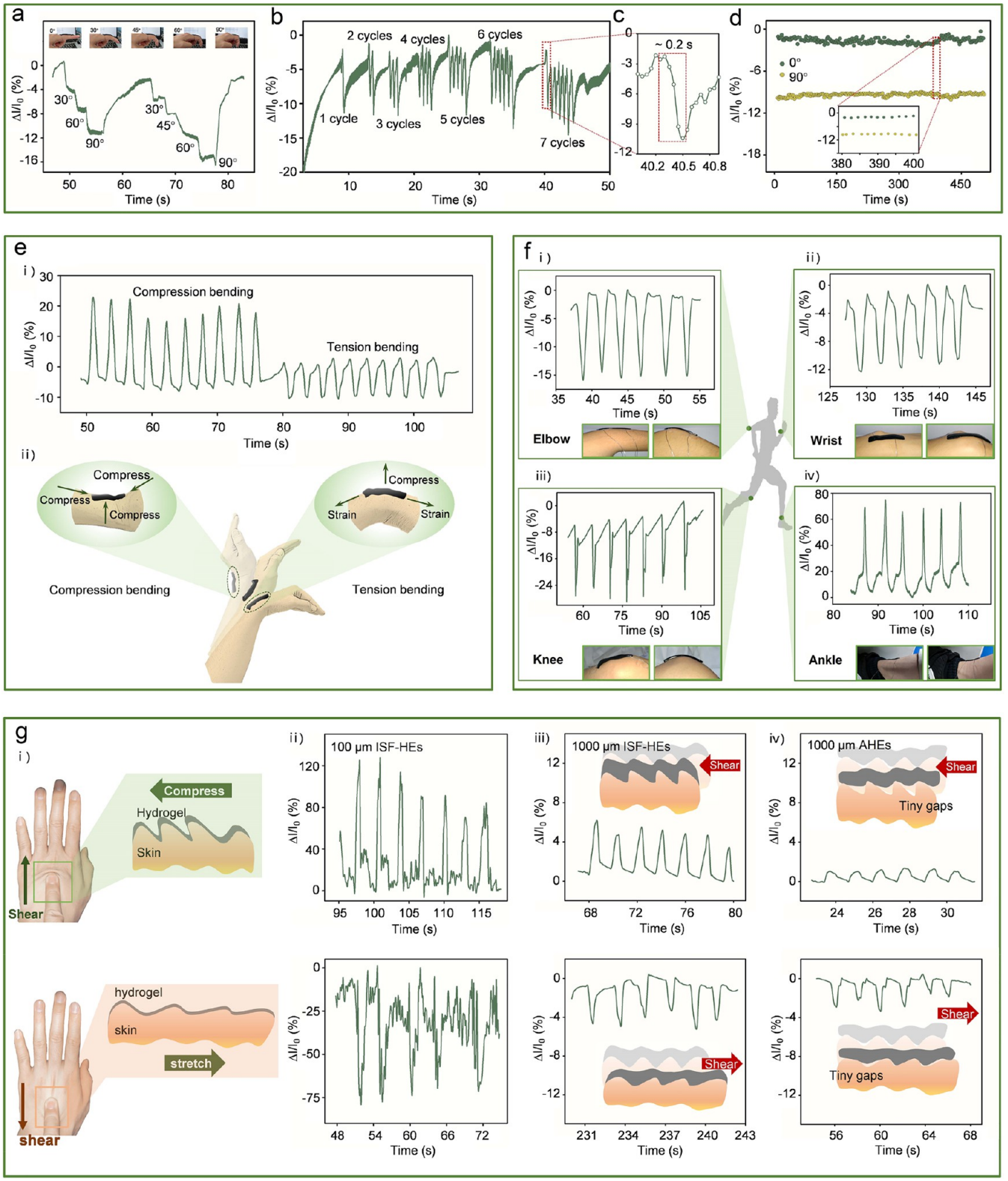

Figure 3. ISF-HEs for human motion monitoring. (a) Relative current change ($\Delta I/I_0$)−time (t) curves obtained by the ISF-HEs, and (b) the rapid and continuous bending actions with (c) a bending response time of 200 ms as well as (d) more than 500 cycles of bending. (e) A simple force analysis of the ISF-HEs on the wrist joint. (f) Overall $\Delta I/I_0$−t curves obtained by the ISF-HEs for monitoring the movement of the elbow (i), wrist (ii), knee (iii), and ankle joints (iv) during human motions. (g) Highly conformal e-skins based on the ISF-HEs for monitoring the shear stress in different directions (i): the ISF-HEs with a thickness of 100 μm (ii) and 1000 μm (iii) as well as the ordinary AHEs (iv).

the wet pig skin stably without falling off after being bent, twisted, and stretched greatly (Figure S14). In addition, the ISF-HEs on the human skin could withstand violent water flushing in a short time due to the high adhesion strength

https://doi.org/10.1021/acsnano.2c03414
ACS Nano XXXX, XXX, XXX−XXX

(Figure 2i(ii)), ulteriorly proving their good performance and potential application in the adhesion of wet interfaces.

Considering the compromise between mechanical properties, electrical conductivity, and interfacial adhesion, the GelMA/PEGDA-CNT-PDA hydrogel with CNT content of 5.0% w/v would exhibit suitable mechanical properties (Young's modulus of 59.31 kPa), electrical conductivity (1.44 $S{\cdot}m^{-1}$), and bioadhesion to meet the requirements of subsequent biosignal acquisition. The cytotoxicity and biocompatibility of the as-prepared ISF-HEs have also been investigated using human immortalized keratinocytes (HaCAT) as model cells for biomedical application. Optical microscope images display that there was no significant difference in the cell numbers and survival status after being cultured in the medium containing different amounts of hydrogel extracts for 24, 48, and 72 h, implying the ideal biocompatibility of the ISF-HEs (Figure S15). The quantitative analysis results of the Cell Counting Kit-8 method also indicated that the ISF-HEs exhibited no visible cytotoxicity in the short term. In addition, HaCAT cells were directly seeded on the surface of the ISF-HEs, and the representative live/dead staining of HaCAT cells also showed that there was no difference in the metabolic viability of cells seeded on ISF-HEs and blank dishes (Figure S15). Further, skin irritation experiments were implemented to demonstrate the histocompatibility of the as-prepared ISF-HEs to skin structures (Figure S16). The ISF-HEs samples were first applied to the dehaired dorsal skin of rats for 3 days, and no obvious erythema was observed on the skin surface after removal. The representative HE-stained histological images displayed that the localized skin with ISF-HEs applied could still maintain the intact and normal tissue structure without distinct inflammatory response, which was the same as the blank skin. In addition, the application of ISF-HEs to human forearm skin did not bring obvious discomfort, no visible erythema or swelling were also observed after at least 6 h, thanks to the good permeability of moisture and air throughout the hydrogel network. All of the above experimental results have demonstrated that the ISF-HEs exhibited ideal biocompatibility and no significant risk of infection and irritation to the intact skin.

ISF-HEs for Human Motion Monitoring. In the daily exercise routine of individuals, real-time and effective acquisition of human biophysical signals (motion posture, heart rate and respiration rate, *etc.*) is very important for the evaluation of exercise status and health condition. Benefiting from the ideal flexibility and elasticity induced resistance changes of the as-prepared ISF-HEs, they could be potentially used as resistance-type stress−strain sensors. The sensing mechanism and performance during being stretched and compressed were first studied. Considering the conductive hydrogel as a conductor in a closed circuit, it is not difficult to understand that the density of CNTs inside the hydrogel respectively decreased and increased under tension and compression within a small deformation, causing the current (I) in the circuit to decrease and increase respectively (Figure S17). The GF was chosen to analyze the strain sensitivity of the hydrogel sensor, which was defined here as the relative current change ($\Delta I/I_0$) against the applied strain (σ) or stress (ε):

$$\mathrm{GF} = \frac{\Delta I}{I_0} \times \frac{1}{\varepsilon \text{ or } \sigma} \tag{1}$$

Similar to the results reported in other literature (Table S2), the GF value of the hydrogel sensor exhibited several stages within the measured strain and stress range. In the low strain range (<50%), the GF value gradually decreased from 1.23 to 0.187 with the stepwise increase in strain. Likewise, the GF value under compression initially stabilized at 0.15 kPa^{-1} when the stress was <2.5 kPa and then decreased to 0.009 kPa^{-1} when the stress increased from 2.5 to 10.15 kPa (Figure S17).

Such ideal stress and strain sensitivity of the as-prepared hydrogel sensor makes it reasonable for body surface motion signal or stimuli monitoring. Therefore, the as-prepared ISF-HEs were firmly attached to different joints to monitor complex human movements in real time. Figure 3a primarily displays that the hydrogel strain sensor could favorably monitor the bending movement of the forefinger with the increasing bending angles from 0° to 90°. The rapid and continuous bending actions could be easily distinguished with a bending response time as low as 200 ms (Figure 3b,c). In addition, after several cycles of bending in a short time (more than 500 times), the current response of the hydrogel sensor at the bending angles of 0° and 90° still remained basically stable near the initial value (Figure 3d). Furthermore, through a simple force analysis of the joint movement (Figure 3e), it is easy to find that the ISF-HEs were mainly stretched or compressed during the tension bending or compression bending of the wrist joint, causing the corresponding resistance to increase or decrease respectively, which was consistent with the resistance changes reported in most literature (Table S3). Accordingly, the self-adhesive ISF-HEs were also utilized to monitor the movement of the elbow, wrist, knee, and ankle joints based on the respective tension bending and compression bending principle (Figure 3f). Apparently, the hydrogel strain sensors could definitely distinguish the respective bending frequency and different movement directions of joint motion. The as-measured relatively smooth signal curves were attributed to the close adhesion of the ISF-HEs to the skin as well as the tissue-like mechanical properties, demonstrating the advantages of the as-prepared hydrogel sensor in artifact-free motion monitoring. The hydrogel sensor could also detect subtle motion changes in the body surface for healthcare application, such as the radial pulse at the wrist and the chest gallery movement during breathing (Figure S18). The heart rate sensor based on the ISF-HEs attached to the wrist could well distinguish the difference in the frequency and amplitude of the radial pulse before and after exercise. Also, the respiratory rate sensor attached to the front chest could monitor the fluctuations of the chest during slow breathing and rapid breathing.

Generally, the thicknesses of the epidermal bioelectronics will affect the conformal contact on the rough biological surface, thereby restricting their normal and endurable functioning in motion monitoring. Specifically, when the thickness was reduced to approximately 100 μm, the highly conformal hydrogel e-skins based on the ISF-HEs could even sense the shear stress in different directions when stretching and squeezing the skin (Figure 3g(i)). The folds and wrinkles on the skin spread out or huddled together, rendering the hydrogel e-skins slightly stretched and compressed (Figure S19), which respectively caused the current response signal to decrease and increase (Figure 3g(ii)). In addition, the conformal ISF-HEs of different thicknesses were all able to feasibly establish mechanical environment-adaptable interfaces on the biological surfaces. Therefore, also for 20% strain of

https://doi.org/10.1021/acsnano.2c03414
ACS Nano XXXX, XXX, XXX−XXX

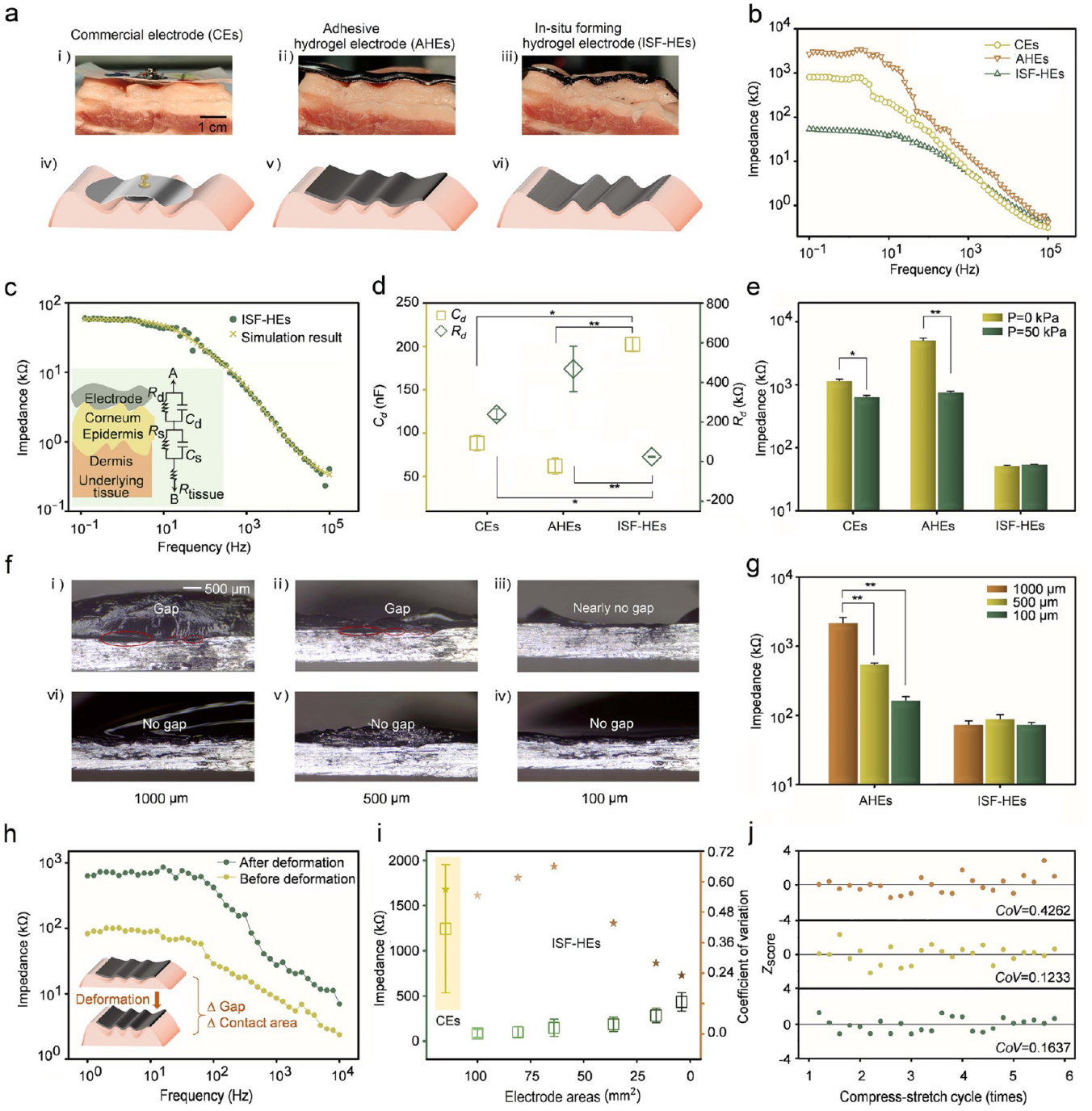

Figure 4. ISF-HEs with relatively low bioelectronic impedance. (a) Contact impedance measurement models of the CEs, AHEs, and ISF-HEs attached to the pigskin. (b) Contact impedance values versus frequency (0.1 Hz to 100 kHz) measured by the CEs, AHEs, and ISF-HEs on the human forearm. (c) Contact impedance values measured by the ISF-HEs as well as the corresponding simulation results. The inset is the simplified LCR circuit model of the electrode-skin interface. (d) Further simulation results of C_d, R_d values at the electrode-skin interface. (e) Differences in the contact impedance values (at 0.1 Hz) measured by three kinds of electrodes before and after applying external pressure. (f) Optical photos of the AHEs and the ISF-HEs with thicknesses of 1000 μm, 500 μm, and 100 μm adhering to the rough metal plates as well as (g) respectively recorded contact impedance values on human forearm skin. (h) Contact impedance values of the hydrogel electrode-skin interface before and after skin deformation. (i) Contact impedance values at 0.1 Hz on human forearm skin, measured by the ISF-HEs with different sizes, as well as their coefficient of variation values after being stretched, compressed and released. The commercial Ag|AgCl electrodes have also been studied incidentally as a control. (j) Standard score (Z_{score}) values of the contact impedance values recorded by the ISF-HEs with thicknesses of 1000 μm, 500 μm, and 100 μm in several compress-stretch cycles. One-factor ANOVA: *, $p < 0.05$; **, $p < 0.01$.

skin, the epidermal ISF-HEs with a thickness of up to 1000 μm could still monitor the horizontal shear deformation of the skin in real time, with an acceptable range of sensitivity reduction (Figure 3g(iii)). The relatively thinner epidermal ISF-HEs could form more small wrinkles that conformed to the stretched or squeezed skin and consequently reveal higher

https://doi.org/10.1021/acsnano.2c03414
ACS Nano XXXX, XXX, XXX−XXX

strain sensitivity to small skin deformations. However, for ordinary adhesive bioelectronics on skin, a comparatively thinner contact layer (A few microns or even thinner) is imminently required to establish a highly compliant electrode-skin interface. A slightly thicker contact interface inevitably tends to introduce more tiny gaps, even under the auxiliary vertical pressure, where the contact compliance is more likely to be weakened by local skin deformation. Hence, when applying the ordinary AHEs based on the prefabricated composite hydrogels with the same thickness of 1000 μm, the measured current response signal level decreased sharply, due to the asynchronous deformation compared with the skin itself (Figure 3g(iv)). Finally, the endurable compliance of the epidermal ISF-HEs to the continuous skin deformation has also been evaluated. When the skin underwent shear deformation in two horizontal directions, the comparatively thinner ISF-HEs (100 μm in thickness) could maintain the current response signal attenuation within 50% after 100 cycles of stretching and squeezing. Contrarily, the current response signal measured by the thicker ISF-HEs (1000 μm in thickness) would gradually attenuate to an indistinguishable level (Figure S19), implying the negative performance and final failure of the thicker electrode-tissue interface to function in the long term. All these measurements have demonstrated that the as-prepared ISF-HEs exhibited excellent response sensitivity, stable and quick responses, repeatable sensing performance for large-scale as well as tiny human motions.

ISF-HEs with Relatively Low Bioelectronic Impedance. Efficiently obtaining high-quality bioelectrical signals from the body surface is also very valuable for exercise status evaluation as well as clinical neurophysiological research. In this case, on-skin electrodes with relatively low contact impedance are also very essential for the collection of sEMG signals with high SNR. The electrode-skin interface model is usually simplified as a parallel circuit of leakage resistance and capacitance (Figure S20). Figure S20 intuitively shows the measurement configuration of the dual-electrode recording electrode-skin impedance. In the ordinary way, for each recording electrode, the electrode-skin impedance should be derived as

$$Z(\omega) = R_s + \frac{R_d/jC_d\omega}{R_d + 1/jC_d\omega} = R_s + \frac{R_d}{1 + j\omega C_d R_d}, \quad \omega = 2\pi f \tag{2}$$

where the resistor R_d represents the charge transfer impedance of the electrode-skin interface, while the capacitance C_d stands for the electric double layer between the electrode and skin. R_s is related to the skin surface conditions and underlying tissues, and R_{tissue} is the resistance of the dermis, subcutaneous tissue layers, and deeper tissues. Therefore, it is not difficult to understand that maintaining high capacitance and low resistance of the electrode-skin interface (eq 2) is very beneficial to reduce the bioelectrical interfacial impedance of on-skin bioelectronics and improves the overall SNR level.

Specifically, Figure 4a displays the commercial Ag|AgCl electrodes (CEs), AHEs, and ISF-HEs attached to the pigskin model for impedance recording. Neither the comparatively stiff CEs nor the ordinary AHEs transferred to the measured sites could conform well to the skin, leaving various tiny or larger gaps with the influx of air or sweat on the uneven skin surface. On the contrary, the epidermal ISF-HEs could better comply with the wrinkled skins. Figure 4b shows the contact impedance values versus frequency (0.1 Hz to 100 kHz) measured with the above three electrodes. The impedance value recorded by the ISF-HEs (about 50 kΩ at 0.1 Hz) was significantly lower than those recorded by the CEs (about 620 kΩ at 0.1 Hz) and ordinary AHEs (about 1.08 MΩ at 0.1 Hz, Figure S21) and was even quite close to the ideal electrode-skin impedance, that is, the inherent impedance of the skin (about 10 kΩ). Such a relatively low electrode-skin impedance not only was related to the hydrogel electrode material with better conductivity than commercial electrodes (Figure S22), but to a large extent depended on the most conformal contact of the epidermal ISF-HEs with the skin. Figure 4c illustrates the complete numerical simulation results of the epidermal ISF-HEs on the human forearm. The measurement results were intensely consistent with an LCR circuit simulation model with R_d = 22.5 kΩ, C_d = 194.6 nF, and R_{tissue} = 179.7 Ω. To highly rationalize the electrode-skin impedance simulation, the stratum corneum and the epidermis with numerous microchannels were simplified as a parallel circuit of R_s (4.3 kΩ) and C_s (43.9 nF). Among these as-established electrode-skin interfaces above, there were definitively the smallest charge transfer resistance (R_d) and the largest capacitance value (C_d) at the *in situ* forming hydrogel electrode-skin interface (Figure 4d). The undesirable and nonclose contact between the ordinary electrode and the skin could be improved by applying auxiliary external pressure. As shown in Figure 4e, after the external pressure of 50 kPa was applied, the contact impedance values collected by the CEs and the AHEs were significantly reduced ($p < 0.05$, 0.01), and the R_d and C_d values obtained by the simulation result also accordingly decreased and increased, respectively. The theoretical analysis of the simplified electrode-skin interface model could draw unanimous conclusions (Figure S23). Otherwise, the contact impedance measured by the epidermal ISF-HEs has not undergone significant fluctuations, manifesting the directly established highly conformal electrode-skin interface without external force intervention.

As mentioned above, the intrinsic thicknesses of the epidermal bioelectronics will determine to a certain extent whether they can primely conform to the wrinkled skins. More specifically, compared with the adhesive hydrogel interface, the epidermal ISF-HEs with thicknesses of 1000 μm, 500 μm, and 100 μm could almost all establish highly conformal interfaces on the rough metal plate, thanks to the strategy of fully penetrating into the gaps and then curing (Figure 4f). Therefore, as shown in Figure 4g, the contact impedance on human skin recorded by the AHEs with the thickness of 100 μm was significantly lower than those of the 500 and 1000 μm thick ones ($p < 0.01$, 0.01). Whereas, there was no significant difference in the contact impedance values of the ISF-HEs (Figure S24).

Furthermore, the real-time measured contact impedance could also be used to evaluate the influence of skin deformation on the compliance of the electrode-skin interface. Before and after skin deformation, changes in the occurring gaps and contact areas between the hydrogel electrode and the curved skin would cause indefinite fluctuations in contact impedance (Figure 4h). First, applying the epidermal ISF-HEs with a collection of different sizes on the human forearm, the measured contact impedance values gradually increased as the electrode areas decreased, but were all far lower than those measured by the CEs. Subsequently, the local skin was cyclically stretched, compressed, and released in the horizontal direction with a strain of 20% (Figure S25), and the measured

https://doi.org/10.1021/acsnano.2c03414
ACS Nano XXXX, XXX, XXX−XXX

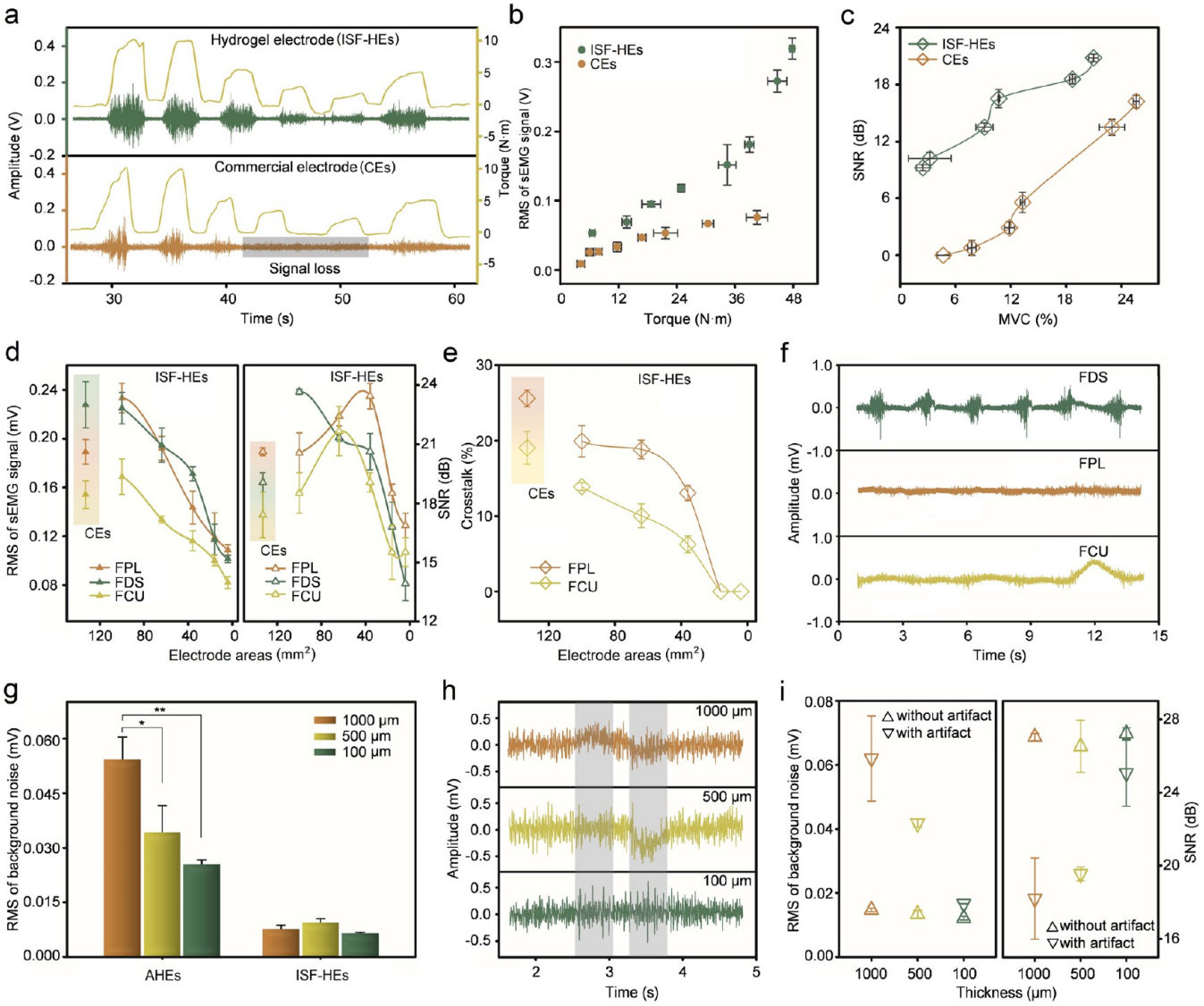

Figure 5. ISF-HEs for high-quality surface electromyography recording. (a) Detailed sEMG signal waveforms continuously measured by the ISF-HEs and the CEs. (b and c) The RMS values and the SNR values of synchronous sEMG signals at various muscle contractions, respectively. (d) Various RMS values and SNR levels of the sEMG signals measured by the ISF-HEs with different sizes. (e) Crosstalk rate (%) of FPL, FCU muscles when only the middle finger moving with the decreasing contact areas of the ISF-HEs. (f) Detailed sEMG signals of FDS, FPL, and FCU muscles when the middle finger moving at a no-crosstalk level. (g) RMS values of background noises recorded by the AHEs and the ISF-HEs. (h) Distorted sEMG signal curves recorded in real time by the ISF-HEs. (i) RMS values of the background noises and SNR levels of the sEMG signals recorded by the ISF-HEs without and with motion artifacts. One-factor ANOVA: *, $p < 0.05$; **, $p < 0.01$.

contact impedance values at 0.1 Hz varied randomly back and forth with skin deformation (Figure S25). The calculated coefficient of variation (CoV) of these impedance values for further analysis are also shown in Figure 4i. As a whole, it is concluded that the ISF-HEs covering smaller contact areas were more likely to maintain the interfacial impedance stability, implying the endurable conformal electrode-skin interface with resistance to motion artifact interference. Moreover, employing the ISF-HEs with different thicknesses on the deformed skin surface, Figure 4j displays the standard score (Z_{score}) of the recorded contact impedance values in several compress-stretch cycles. The CoV values of the measured contact impedance by the relatively thinner ISF-HEs with thicknesses of 500 and 100 μm were both lower than that of the 1000 μm-thick hydrogel electrodes (Figure S26), suggesting the more stable and endurable electrode-skin interfaces established by the thinner hydrogel layers.

Considering the endurance and susceptibility of epidermal electronics in the unstable surrounding environment, it is worth exploring the influence of varying hydrated conditions on the sensing performance, especially for hydrogel bioelectronics exposed to air. Actually, hydrogel bioelectronics are prone to lose water, thereby impairing the flexibility and compliance of the electrode-tissue interface. Figure S27 displays the real-time contact impedance values measured by ISF-HEs during the dehydration and rehydration process (3 h). As the ISF-HEs continuously lost water, the values of measured contact impedance gradually increased. Nevertheless, once the ISF-HEs were rehydrated by spraying water, the local interfacial impedance would basically return

https://doi.org/10.1021/acsnano.2c03414
ACS Nano XXXX, XXX, XXX−XXX

to the original level. This reversible interfacial impedance variation would be attributed to the reconstruction of the highly conformal electrode-tissue interface. Further, the measurement paradigms, such as the configuration of lead wires, are strongly associated with the sensing performance and stability of the ISF-HEs. For the ISF-HEs with lead wires buried in it, or placed on it, the real-time contact impedance values measured by the former could stabilize at the initial level for a longer time (about 60 min) than the latter (about 30 min), thanks to the slower water loss of the inner hydrogel than the surface (Figure S27). Therefore, the ISF-HEs with lead wires buried in it, sprayed with water approximately every 30 min, were able to acquire the stable biological signals regardless of the dehydrating environment. All in all, these experimental measurements demonstrated the feasibility of the ISF-HEs being applied to the wrinkled skin as well as the advantages over commercial electrodes in terms of the ultralow bioelectronic impedance and the long-term stability. Integrating this technology with other exciting theragnostics, we can better improve human health.[32−37]

ISF-HEs for High-Quality Surface Electromyography Recording. To the best of our knowledge, the as-prepared ISF-HEs possess relatively ultralow bioelectronic impedance compared with most reported wet hydrogel electrodes, indicating their outstanding advantages in the surface bioelectrical signal acquisition with high amplitude and high SNR. Therefore, the epidermal ISF-HEs were used to record the real-time synchronous sEMG signals of the biceps brachii at different voluntary contractions (Figure S28). Figure 5a displays the synchronized sEMG signals respectively measured by the ISF-HEs and the CEs with muscle activity within 10 N·m torque. It is recognized that the measurement limit of the sEMG signal recorded by the ISF-HEs was at least as low as the muscle activity of 1.5 N·m torque, while the sEMG signal measured by the CEs under the muscle activity of 4.5 N·m torque showed an obvious signal loss. Furthermore, Figure 5b exhibits the quantitative relationships between the applied torque and the root-mean-square (RMS) values of synchronous sEMG signal. All these results have distinctly manifested that the ISF-HEs were more sensitive than the CEs at various muscle contractions. Besides, as shown in Figure 5c, the ISF-HEs possessed larger SNR levels than the CEs, especially at relatively slight muscle contractions below 6% maximal voluntary contraction (MVC, total MVC was obtained from the maximal applied torque in Figure S28). Such high SNR levels will be considered to be extremely beneficial for subtle muscle activity monitoring as well as for further physical human-robot interaction and prosthetic control.

Signal crosstalk contamination and motion artifact interference are both urgent problems to be solved for high-quality sEMG signal acquisition. The signal crosstalk originates from the adverse interaction between closely adjacent muscle units in spatial distribution, resulting in the serious misinterpretation of the overall sEMG signal recorded by epidermal electrodes with lower spatial resolution. Presently, the method of reducing the contact area of the epidermal electrode is generally adopted to minimize the signal crosstalk, but meanwhile the amplitude and the SNR of the collected sEMG signal are also unfortunately weakened. Herein, the ISF-HEs with different contact areas were used to collect the sEMG signal of flexor pollicis longus (FPL), flexor digitorum sublimis (FDS), and flexor carpi ulnaris (FCU) of human forearm in real time (Figure S29). As shown in Figure 5d, the RMS values and SNR levels of the sEMG signals, respectively, recorded by the ISF-HEs with gradually decreased contact areas on three separate muscles all maintained similar downward trends as a whole. In addition, when flexing the thumb, flexing the middle finger, and flexing the little finger with adduction of palm, respectively, the crosstalk rates of their corresponding sEMG signals were calculated for further research (Figure S30). As described in Figure 5e, the target muscle activity here would arise from the middle finger movement, and the crosstalk signals were also recorded synchronously on FPL and FCU muscles. Obviously, as the contact areas of the ISF-HEs decreased, the crosstalk rates of FPL and FCU muscles gradually decreased, eventually reaching a negligible level with a size of 4 mm × 4 mm. Specifically, Figure 5f exhibits the synchronously collected sEMG signals of FDS, FPL, and FCU muscles when the middle finger moved at a no-crosstalk level. All these results have adequately demonstrated the advantages of the as-prepared ISF-HEs in minimizing signal crosstalk while maintaining a high SNR level.

Motion artifact interference is quite ubiquitous and even more serious in wearable electronics. In the previous analysis, it has been proved that the motion artifacts are largely caused by the skin deformation induced undesirable changes in the impedance of the electrode-skin interface. The contact compliance and interfacial impedance variations of the electrode-skin interface during motion are associated with the inherent thickness of the hydrogel interface. As depicted in Figure 5g, the RMS values of the sEMG signal background noise recorded by the AHEs with thicknesses of 500 and 100 μm were significantly lower than that of the 1000 μm-thick hydrogel electrode ($p < 0.05, 0.01$). For the ISF-HEs, the RMS values of the background noise were all kept at a low level, implying the highly conformal hydrogel electrode-skin interface regardless of the hydrogel layer thickness (Figure S31). Afterward, the definite effects of motion artifacts on real-time sEMG signal acquisition were also studied. Figure 5h shows the detailed sEMG signals when the ISF-HEs were subjected to a vertical 50 kPa external pressure. The gray areas of interest severally indicated the application and removal of 50 kPa external pressure. At the moment of external force, there were both abnormal deviations in the real-time sEMG signal curves collected by the ISF-HEs with the thicknesses of 1000 and 500 μm. Especially after the local skins underwent several cycles of squeezing, stretching, and releasing, the real-time sEMG signal curves recorded by the 100 μm-thick ISF-HEs showed the least distortion before and after the applied external pressure (Figure S32). Moreover, the RMS values of the sEMG signal background noises, recorded by the 1000 and 500 μm-thick ISF-HEs under the motion artifact interference, were both observably higher than those without motion artifacts, while the changes in SNR were just the opposite (Figure 5i). And objectively speaking, for the thinnest ISF-HEs with the thickness of 100 μm, the increase in the RMS value of the recorded sEMG signal background noises was indeed negligible, and the minimized SNR level was also acceptable compared with the other two ones (Figure S33). All these measurements have manifested that the comparatively thinner epidermal ISF-HEs were more likely to reveal no evident susceptibility to the skin deformations or motion artifacts. The as-prepared ISF-HEs were also utilized to monitor the human electrocardiography (ECG) signal (Figure S34). The real-time measured ECG signal showed easily distinguishable P wave,

https://doi.org/10.1021/acsnano.2c03414
ACS Nano XXXX, XXX, XXX−XXX

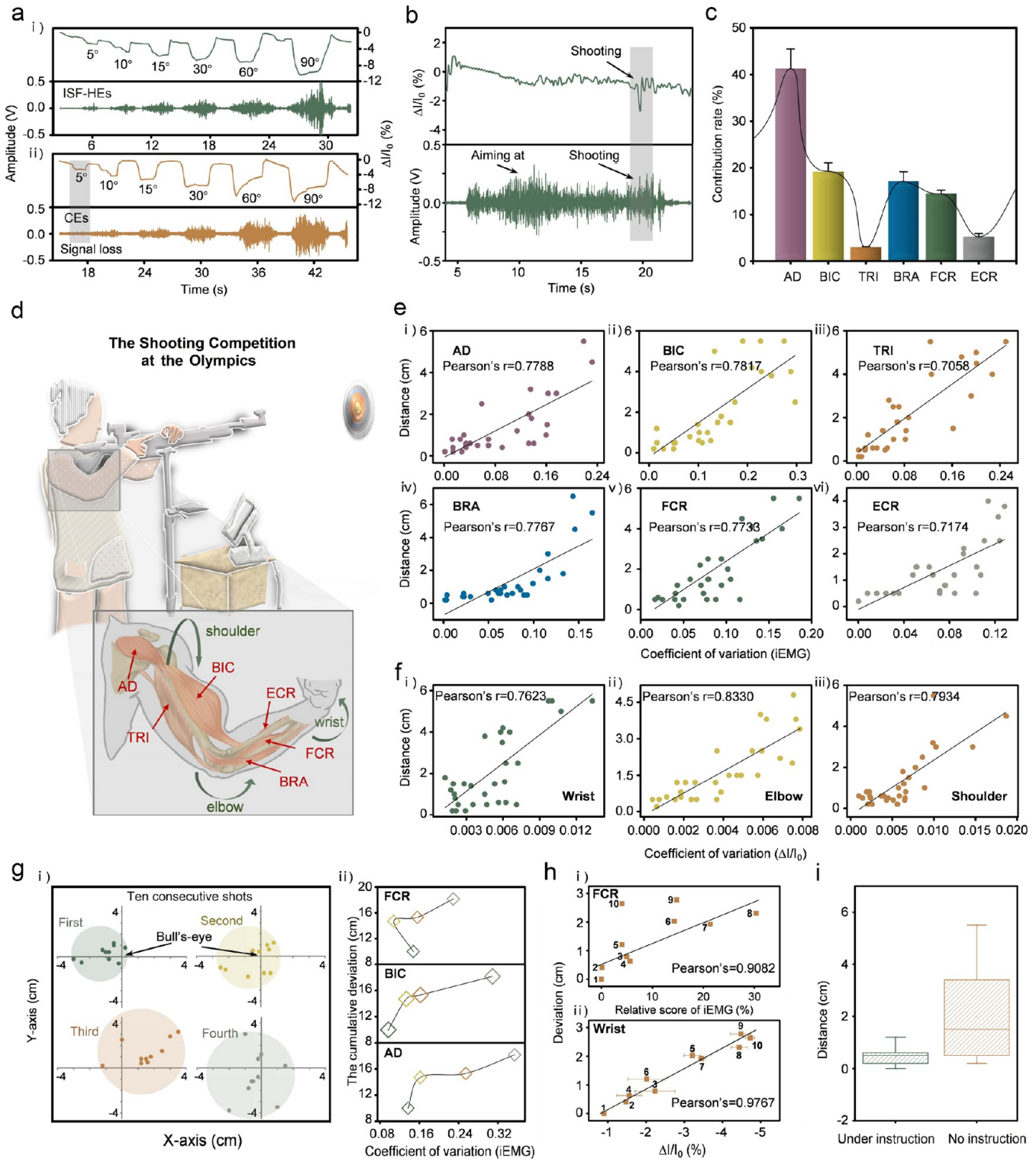

Figure 6. Wearable motion and electromyography monitoring for the comprehensive exercise assessment. (a) Real-time sEMG signals of the biceps brachii muscle collected by the ISF-HEs (i) and the CEs (ii) as well as the current response signals caused by the elbow joint bending. (b) Detailed sEMG signals of the flexor carpi radialis muscle and the current response signals caused by the wrist joint bending during the complete aiming and shooting process. (c) Contribution rates of the six main muscles in the aiming process. (d) Comprehensive shooting assessment system based on the application of the ISF-HEs to simultaneously monitor the main muscle activities of the right arm with a rifle, as well as the joint bending movements during the shooting process. (e and f) Studies of the shooting accuracy in a single shot. (g) Location distribution of the 10 impact points of the consecutive multiple shots (i) and the quantitative analysis results of the cumulative deviations and the CoV values of the iEMG of the FCR, BIC and AD muscles before each trigger (ii). (h) Linear regression analysis between the shooting precision and the stability of muscle activity (i) and joint movement stability (ii) during the consecutive multiple shots. (i) Comparison of the shooting results between the special shots under the guidance of the shooting process assessment system and the random shots under no guidance.

https://doi.org/10.1021/acsnano.2c03414
ACS Nano XXXX, XXX, XXX−XXX

QRS complex and T wave, from which some essential health information such as heart rate, R-R interval and R-wave amplitude could be analyzed quantitatively.

Wearable Motion and Electromyography Monitoring for the Comprehensive Exercise Assessment. As a proof-of-concept of wearable hydrogel device, the ISF-HEs would possess superior performance over the CEs and AHEs in motion monitoring and surface electromyography signal acquisition. Furthermore, simultaneous motion and sEMG monitoring have also been performed for highly comprehensive and more reasonable exercise or health status evaluation, taking shooting sports as an example. The shooting competition (such as air rifles) is a common event in the Olympics and usually holds strong requirements for ideal movement stability as well as elaborate motion control and balance abilities of the athletes. Herein, a shooting assessment system based on fine motion and relevant muscle activity monitoring was developed, to analyze the relationship between the continuous and stable movement during aiming and triggering process and the shooting scores and also for subsequent shooting training guidance. Primarily, Figure 6a displays the elbow joint movement and the real-time sEMG signals of the biceps brachii muscle collected simultaneously by the ISF-HEs and the CEs, respectively. Obviously for sEMG signal acquisition, the ISF-HEs were more sensitive to the joint bending motions at small angles thanks to the overall higher SNR levels, while the CEs showed unexpected sEMG signal loss at the bending of 5°. In addition, it is not difficult to expressly distinguish pivotal moments and actions such as starting to aim and triggering during the shooting, because of the sudden fluctuations of sEMG and motion signals caused by temporary muscle activity (Figure 6b). The above analyses have specifically proved the feasibility of the ISF-HEs for real-time shooting process monitoring.

Subsequently, a comprehensive shooting assessment system was established, through the application of the ISF-HEs to simultaneously monitor the main muscle activities of anterior deltoid (AD), biceps brachii (BIC), triceps brachii (TRI), brachioradialis (BRA), flexor carpi radialis (FCR), and extensor carpi radialis (ECR) muscles of the right arm with a rifle as well as the bending movements of the shoulder, elbow, and wrist joints during the shooting process (Figure 6d). Then the complete courses of the single shot and consecutive multiple shots have been carefully monitored and further evaluated. Figure 6c shows the contribution rates of the main muscles in the aiming process, indicating that holding the rifle steadily with both arms was largely associated with the AD, BIC, and FCR muscles. The integral EMG (iEMG) is the total amount of discharge of muscle motor units participating in the activity within a certain period of time, and its values could seriously reflect the number of motor units and the discharge volume of each motor unit. Thus, here the variation degree of iEMG values in the 3 s before triggering was applied to evaluate the main muscle activity stability of the right arm (Figure S35). First of all, the significant issue of shooting accuracy during a single shot was studied. The shooting accuracy parameter was equivalently defined as the distance between the bullet's hitting point on the target and the bull's eye. Figure 6e primarily shows the different CoV values of the iEMG of the six major muscles within 3 s before triggering and the corresponding shooting results (distances). Generally, a relatively larger CoV value of the iEMG, implying the more inconsistent and fluctuant muscle activity within 3 s, would cause the hitting point to deviate further from the bull's eye. Further linear regression analysis results display that there was a strong correlation between the CoV values of the iEMG of the main muscles and the shooting scores (distances), all with the Pearson coefficients >0.7 (Figure S36). In addition, there was also a similar correlation between the CoV values of the current response signal caused by the joint motion within 3 s before triggering and the shooting scores (distances), all with the Pearson coefficients >0.7 (Figure 6f). Furthermore, according to the slope values of the regression equations, the muscle activity of BRA, FCR, and ECR muscles on the forearm of the shooter as well as the wrist joint movement stability would certainly leave greater impacts on the shooting accuracy.

Afterward, the other noteworthy issue of shooting precision during the consecutive multiple shots was also studied. Figure 6g(i) visually shows the absolute location distributions of the bullets hitting the target for 10 consecutive shots after a single aiming, from which it can be clearly deduced that the concentration of the impact point distributions was positively equivalent to the shooting accuracy. For the consecutive multiple shots, the overall shooting performance could be described as the cumulative deviations between the impact point of the first bullet and the impact points of the remaining nine bullets. As displayed in the quantitative analysis, there was an approximately positive correlation between the cumulative deviations and the CoV values of the iEMG of the FCR, BIC, and AD muscles before each trigger (Figure 6g(ii)). Apparently, the stable and consistent muscle activities would be intensively involved with not only the single shot accuracy but also the overall shooting precision of multiple shots, and the latter likewise showed more susceptibility to the FCR muscle activity of the forearm compared to the other ones of the upper arm (BIC) and the shoulder (AD). Besides, Figure 6h exhibits the several deviations between each impact point and the impact point of the first bullet, with the relative scores of the iEMG within 3 s before each trigger to the iEMG of the first shot (Figure S38), and the current response signals caused by the wrist joint motion (Figure S39). Both the relative scores of iEMG and the current response signals would maintain a strong linear correlation with the deviations, with the Pearson coefficients even >0.9. Appreciably, the bullets fired later in the shooting sequence were likely to deviate further from the first impact point in position, which might be associated with the gradual decrease in muscle activity and motion stability caused by muscle fatigue in the later period. Taken together, all these measurements and analyses have fully proved the feasibility and practicality of the as-prepared ISF-HEs in reasonable estimation of the shooting accuracy for the single shot and the shooting precision for the consecutive multiple shots. Finally, the shooting assessment system established above was used for preliminary shooting training guidance, regarding the relatively small CoV values of the iEMG within 3 s, such as <0.05, as a judgment criterion for the stability of muscle activity (Figure S40). Accordingly, the overall distances between the impact point and the bull's eye when triggering at the special moment were distinctly lower than those when triggering at a random moment during the aiming process, implying the superior shooting performance or scores under instruction (Figure 6i).

CONCLUSIONS

In this research, an innovative design strategy for epidermal bioelectronics has been proposed, to establish the bioelectronic coupling and mechanical adaptable interface on the wrinkled

https://doi.org/10.1021/acsnano.2c03414
ACS Nano XXXX, XXX, XXX−XXX

biological surface through the *in situ* forming method, instead of the conventional adhesive approach. Based on this principle, a highly adhesive and conformal hydrogel interface was formed *in situ* on the rough skin surface, by the near-infrared (NIR) light induced one-step thermal cross-linking of the premixed precursor aqueous solutions. The ISF-HEs would have superior compliance with the curved skin, regardless of the microstructure obstacles such as wrinkles and hair, and thus could monitor large-scale as well as tiny human motions with excellent sensing properties. The highly conformal hydrogel electrode-skin interface would exhibit relatively lower bioelectronic impedance than other reported wet and dry electrodes as well as the long-term contact stability with resistance to skin deformation. Additionally, the ISF-HEs could be applied to collect high-quality sEMG signals, with the higher SNR level, minimized signal crosstalk, and antimotion artifact interference performance, compared with the CEs and AHEs.

Furthermore, simultaneously human motion and sEMG monitoring have also been carried out for the assessment of exercise status, taking the common shooting sports for example. All these analyses of the motion and muscle activity stability have fully demonstrated the feasibility of the as-prepared hydrogel bioelectronics in the reasonable estimation of the shooting accuracy or precision for the single shot as well as the consecutive multiple shots. In conclusion, we have successfully established a highly conformal hydrogel electrode-tissue interface on the biological surface through the *in situ* forming strategy, which will provide more ideas for the design of advanced epidermal bioelectronics (Table S4). It is believed that in the near future, the epidermal ISF-HEs will also be widely used in the fields of health assessment, prosthesis control, as well as brain-computer interface, *etc.*

EXPERIMENTAL SECTION

Materials and Chemicals. Gelatin (type A from the porcine skin, ~250 g Bloom), poly(ethylene-glycol) diacrylate (PEGDA, average molecular weight ~600), and dopamine hydrochloride (DA) were all obtained from Aladdin (Shanghai, China). Methacrylic anhydride (MA) was obtained from Aldrich Chemical Reagent Company. Multiwalled carbon nanotube (CNT, NC7000) was purchased from Nanocyl S.A., and its average diameter, average length, specific surface area, and purity are 9.5 nm, 1.5 μm, 250−300 $m^2 \cdot g^{-1}$, and 90%, respectively. Potassium peroxodisulfate ($K_2S_2O_8$) and sodium bisulfite ($NaHSO_3$) were supplied by Sinopharm Group Chemical Reagent Co. LTD (Guangzhou, China). Unless otherwise specified, all reagents are of analytical grade, and all solutions are prepared with deionized water.

Preparation of Composite Conductive Hydrogels. *Synthesis of GelMA.* Five g of gelatin was added to 50 mL of PBS (0.01 M, pH = 7.2), stirred continuously at 60 °C until completely dissolved. Then 4 mL of MA was added dropwise to the above solution, followed by stirring at 60 °C for 6 h. Afterward, the resulting mixed solution was dialyzed in deionized water for 4 days. Finally, the obtained sample solution was freeze-dried for use.

Prepolymerization of DA. Polydopamine (PDA) chains were obtained through an alkali-induced oxidation and self-polymerization of dopamine hydrochloride (DA). DA powder was dispersed in a vial containing tris-HCl buffer (pH = 8.5) and 5 mM $K_2S_2O_8$ and then oxidized and self-polymerized at room temperature for 1 h.

Hydrophilic Modification of CNTs. The well-dispersed CNTs in water were obtained by acid treatment. Specifically, 1 g of CNTs and 40 mL of sulfuric acid (98%) and nitric acid (70%) mixed solution (volume ratio 3:1) were added to the round-bottom flask, refluxed, and stirred at 60 °C for 6 h. Then a large amount of deionized water was added to dilute the mixed solution after cooling and removed the supernatant after standing overnight. The precipitate was redispersed in deionized water for several centrifugal concentrations, and finally the resulting solution was diluted to 10 mL to obtain a 10 wt% CNT aqueous dispersion.

Preparation of Composite Conductive Hydrogels. The conductive hydrogel was obtained by a facile one-step method of near-infrared light-induced thermal cross-linking. GelMA (10% w/v), different amounts of PEGDA, CNT aqueous dispersion, and PDA prepolymer solution were mixed thoroughly under stirring to obtain a uniformly dispersed conductive mixture. Then the initiator system $K_2S_2O_8$ (40 mM)-$NaHSO_3$ (20 mM) was added to the above solution, and finally the mixed solution was exposed to the infrared physiotherapy lamp for about 100 s to obtain the GelMA/PEGDA-CNT-PDA conductive composite hydrogel. The luminous power and working distance of the physiotherapy lamp could be adjusted as required.

Characterization of Composite Conductive Hydrogels. Morphology of composite conductive ink was characterized by a transmission electron microscope (TEM, JEM-1400). The surface structure of the GelMA/PEGDA-CNT-PDA hydrogels was examined by a scanning electron microscope (SEM, ZEISS-AURIGA). The ^{1}H NMR spectra of GelMA were analyzed to investigate interactions between gelatin and MA. The Fourier transform infrared (FT-IR) analyses of GelMA/PEGDA and GelMA/PEGDA-CNT composites were examined to search for the internal chemical structure of the complexes.

Mechanical Testing. The mechanical properties of GelMA/PEGDA-CNT-PDA hydrogels were evaluated by carrying out their strain−stress tests using a universal material testing machine (LR10K Plus). Standard test samples (40 mm in length, 10 mm in width) were clamped at the stage and stretched at a tensile speed of 20 $mm \cdot min^{-1}$. The step loading−unloading tests were performed at multistep strains of 15%, 30%, 45%, 60%, 75%, and 90%. The cyclic loading−unloading tests were conducted with the strain of 60% for 20 cycles.

Conductivity Measurement. The cyclic voltammetry (CV) curves and electrochemical impedance spectra (EIS) were obtained from an electrochemical analyzer (CHI627D, Shanghai Chenhua, China) and an electrochemical workstation (Versa STAT 4). The conductance (σ) of the GelMA/PEGDA-CNT-PDA hydrogels with different CNT content was measured and calculated by a digital multimeter as follows:

$$\sigma = \frac{1}{R} \times \frac{L}{S} \tag{3}$$

where L, S, and R represent the length, cross-sectional area, and resistance values read directly from the digital multimeter.

Adhesion Tests. The adhesive strength of the GelMA/PEGDA-CNT-PDA hydrogels was measured by performing their tensile adhesion testing using a universal material testing machine (LR10K Plus). The hydrogels were placed on glass stages, and the stages were pulled at a speed of 5 $mm \cdot min^{-1}$ until the hydrogels broke or fell off the glass.

Cytotoxicity and Biocompatibility Studies. Human immortalized keratinocytes (HaCAT) were chosen to investigate the biocompatibility of the GelMA/PEGDA-CNT-PDA hydrogels. The as-prepared composite hydrogels were sterilized by autoclaving and immersed in culture medium for 24 h, and the culture medium was filtered and diluted to obtain the medium containing different amounts of hydrogel extracts. After the cells were cultured in the medium for 24, 48, 72 h, the cell survival status and number were observed using an inverted fluorescence microscope (Nikon, ECLIPSE Ti-u), and the cell viability was analyzed by the Cell Counting Kit-8 method using a microplate reader (450 nm). HaCAT cells were also directly seeded on the composite hydrogel surface, and live/dead staining (Calcein AM/PI Double Stain Kit) was used to detect the cell metabolic viability. The selected GelMA/PEGDA-CNT-PDA hydrogel: GelMA (10% w/v), PEGDA (5% w/v), CNT (5% w/v), PDA (5 wt% DA/GelMA). For animal skin irritation experiments, two ISF-HEs with a diameter of 1.0 cm were applied to the dehaired dorsal skin of rat for 3 days. The localized skins of interest were excised and fixed in 4%

https://doi.org/10.1021/acsnano.2c03414
ACS Nano XXXX, XXX, XXX−XXX

paraformaldehyde for 48 h, followed by paraffin embedding, sectioning, and hematoxylin and eosin staining for histological analyses. The animal use protocol has been reviewed and approved by the Institutional Animal Care and Use Committee (IACUC), Sun Yat-Sen University (approval no.: SYSU-IACUC-2019-000191).

ISF-HEs for Human Motion Monitoring. These experiments on human subjects were approved by the Ethics Committee of the Guangdong Work Injury Rehabilitation Center (no. AF/SC-07/2017.10). All procedures were conducted according to the Declaration of Helsinki. The NIR light induced *in situ* forming highly conformal GelMA/PEGDA-CNT-PDA hydrogels were used as epidermal hydrogel bioelectronics. First, the foam tape cut into a round or square shape was tightly applied to the skin surface to act as a mold for *in situ* forming of the hydrogels. Second, the composite conductive ink was carefully transferred to the mold through a syringe or 3D printer. Finally, the conductive ink was directly exposed to the NIR light until the hydrogel was formed, and then the previous foam tape mold was removed. The lead wires to external devices were buried in or under the ISF-HEs and sprayed with water about every 30 min, for human motion monitoring as well as the bioelectronic impedance acquisition and sEMG recording.

For human motion monitoring, the epidermal ISF-HEs were directly formed *in situ* at the finger, wrist, elbow, knee, and ankle to monitor the corresponding joint movement; the ISF-HEs were also formed at the wrist and the front chest to monitor the radial pulse and breathing rhythm. All $\Delta I/I_0-t$ curves were obtained through electrochemical workstation (CHI627D, Chenhua, Shanghai, China):

$$\Delta I/I_0 = \frac{I - I_0}{I_0} \tag{4}$$

where I represents the real-time current and I_0 represents the initial current value.

Bioelectronic Impedance Measurements. The contact impedance of the electrode-skin interface was measured through a two-electrode configuration on the forearm by the electrochemical workstation (Versa STAT 4). The ISF-HEs were also prepared by the NIR light induced one-step thermal cross-linking of the premixed precursor aqueous solutions. The ordinary AHEs were applied by adhering the preformed GelMA/PEGDA-CNT-PDA composite conductive hydrogels to the forearm. The disposable commercial AglAgCl electrodes (CEs) were purchased from Shanghai Shenfeng Medical & Health Articles Co. Ltd. and used directly without other treatment. The circuit model of the electrode-skin interface was simulated by the ZSimDemo software.

For the antimotion artifact interference measurements, the local skin was successively stretched, compressed, and released to undergo a strain of 20% in the horizonal direction. The coefficient of variation (CoV) is defined as the ratio of the standard deviation of the samples to its mean value. The standard score (Z_{score}) is defined as the deviation of the several variable values from its mean value divided by the standard deviation.

Surface Electromyography Acquisition. For surface electromyography (sEMG) signal acquisition, the three-electrode systems of two recording electrodes attached to the muscle abdomen regions with a center-to-center distance of 2.0 cm and one reference electrode attached to the end of muscles were used here for all sEMG signal acquisitions. The epidermal ISF-HEs, AHEs, and CEs were all applied for comparative analysis.

For the SNR levels analysis, the two recording electrodes with a diameter of 1 cm and a center-to-center distance of 2 cm were attached to the bellies of biceps brachii muscle, and a ground electrode was attached to the end of muscles. The sEMG signals were recorded by a homemade eight-channel EMG collector with a gain of 4000 and then sampled by the digital-analog conversion (DAQ-6341, National Instruments, Austin, TX, USA) with a sampling frequency of 1000 Hz and a resolution of 16 bits.

For sEMG signal crosstalk tests, the two recording electrodes with different sizes of 10 mm × 10 mm, 8 mm × 8 mm, 6 mm × 6 mm, 4 mm × 4 mm, and 2 mm × 2 mm as well as a center-to-center distance of 2 cm were attached to the bellies of flexor pollicis longus (FPL), flexor digitorum sublimis (FDS), and flexor carpi ulnaris (FCU) muscles of human forearm, and a ground electrode was attached to the end of muscles. The sEMG signals were measured by a multichannel physiological recorder (MP160, BIOPAC Systems, Inc., USA) based on the EMG100C amplifier.

For the antimotion artifact interference measurements, the local skin was successively stretched, compressed, and released to undergo a strain of 20% in the horizontal direction. The recording electrodes with a size of 6 mm × 6 mm, different thicknesses of 1000 μm, 500 μm, 100 μm, and a center-to-center distance of 2 cm were attached to the bellies of biceps brachii muscle, and the ground electrode was attached to the end of muscles. The sEMG signals were measured by a multichannel physiological recorder (MP160, BIOPAC Systems, Inc., USA) based on the EMG100C amplifier.

For the electrocardiogram (ECG) signal acquisition, three electrodes were fixed on the left lower limb (wrist), right upper limb (wrist), and right lower limb (ankle), respectively. The ECG signals were measured by a multichannel physiological recorder (MP160, BIOPAC Systems, Inc., USA) based on the ECG100C amplifier.

Simultaneous Motion and sEMG Monitoring for the Comprehensive Exercise Assessment. For the comprehensive shooting assessment system, the as-prepared ISF-HEs were applied to simultaneously monitor the main muscle activities of anterior deltoid (AD), biceps brachii (BIC), triceps brachii (TRI), brachioradialis (BRA), flexor carpi radialis (FCR), and extensor carpi radialis (ECR) muscles of the right arm with a rifle as well as the bending movements of the shoulder, elbow, and wrist joints during the shooting process. For the shooting accuracy estimation for a single shot, the shooter held the rifle toy model in both hands, standing 3 m away from the target. The stability of muscle activity was described by the CoV values of the iEMG of the first, the second, and the third second before triggering, and the stability of joint motion was described by the CoV values of the current response signal caused by the joint motion. The shooting accuracy was equivalently defined as the distance between the impact point and the bull's eye. For the shooting precision assessment for the consecutive multiple shots, the shooter would fire 10 consecutive bullets after a single aim, with an interval of 5 s each time. The stability of muscle activity was described by the CoV values of the iEMG within 3 s before each trigger, and the shooting precision was equivalently defined as the cumulative deviations between each impact point and the impact point of the first bullet.

ASSOCIATED CONTENT

Supporting Information

The Supporting Information is available free of charge at https://pubs.acs.org/doi/10.1021/acsnano.2c03414.

Additional experimental details, including preparation and synthesis of hydrogels, and protocols and statistical methods for subsequent epidermal bioelectronics; Figures S1−S40: Supplementary experimental results in preparations of hydrogel bioelectronics, human motion monitoring, interfacial impedance acquisition, sEMG recording, *etc.*; Tables S1−S4: Performance comparison between as-prepared hydrogel bioelectronics and other reported literatures (PDF)

AUTHOR INFORMATION

Corresponding Authors

Hong-qi Xia − *Key Laboratory of South Subtropical Fruit Biology and Genetic Resource Utilization, Ministry of Agriculture and Rural Affairs, Institute of Fruit Tree Research, Guangdong Academy of Agricultural Sciences, Guangdong Provincial Key Laboratory of Tropical and*

https://doi.org/10.1021/acsnano.2c03414
ACS Nano XXXX, XXX, XXX−XXX

Subtropical Fruit Tree Research, Guangzhou 510640, China; Email: xiahongqi@gdaas.cn

Xingcai Zhang − *School of Engineering and Applied Sciences, Harvard University, Cambridge, Massachusetts 02138, United States; School of Engineering, Massachusetts Institute of Technology, Cambridge, Massachusetts 02139, United States*; orcid.org/0000-0001-7114-1095; Email: xingcai@mit.edu

Jianhua Zhou − *Key Laboratory of Sensing Technology and Biomedical Instruments of Guangdong Province, School of Biomedical Engineering, Sun Yat-sen University, Guangzhou 510275, China; Division of Engineering in Medicine, Department of Medicine, Brigham and Women's Hospital, Harvard Medical School, Cambridge, Massachusetts 02139, United States*; orcid.org/0000-0001-9895-8679; Email: zhoujh33@mail.sysu.edu.cn

Authors

Hao Tang − *Key Laboratory of Sensing Technology and Biomedical Instruments of Guangdong Province, School of Biomedical Engineering, Sun Yat-sen University, Guangzhou 510275, China*

Yuanfang Li − *Key Laboratory of Sensing Technology and Biomedical Instruments of Guangdong Province, School of Biomedical Engineering, Sun Yat-sen University, Guangzhou 510275, China*

Baiqi Chen − *Key Laboratory of Sensing Technology and Biomedical Instruments of Guangdong Province, School of Biomedical Engineering, Sun Yat-sen University, Guangzhou 510275, China*

Xing Chen − *School of Engineering and Applied Sciences, Harvard University, Cambridge, Massachusetts 02138, United States*; orcid.org/0000-0001-9735-0979

Yulong Han − *School of Engineering and Applied Sciences, Harvard University, Cambridge, Massachusetts 02138, United States; School of Engineering, Massachusetts Institute of Technology, Cambridge, Massachusetts 02139, United States*

Ming Guo − *School of Engineering, Massachusetts Institute of Technology, Cambridge, Massachusetts 02139, United States*

Rong Song − *Key Laboratory of Sensing Technology and Biomedical Instruments of Guangdong Province, School of Biomedical Engineering, Sun Yat-sen University, Guangzhou 510275, China*

Complete contact information is available at: https://pubs.acs.org/10.1021/acsnano.2c03414

Author Contributions

H.T. designed projects, carried out experiments, analyzed experimental results and data, and wrote the manuscript. Y.L., B.C., X.C., and Y. H. carried out experiments and analyzed experimental results and data. R.S. provided the equipment and instrument support. J.Z., H.X., X.Z., and M.G. provided guidance on experiments and data analysis and reviewed and revised the manuscript. J.Z. and X.Z. conceived the study, supervised the research, and reviewed and revised the manuscript. J.Z. offered funding support. All authors have participated in the scientific research and manuscript comments.

Notes

The authors declare no competing financial interest.

ACKNOWLEDGMENTS

This work was partially supported by Guangdong Basic and Applied Basic Research Foundation (2019A1515111183), National Natural Science Foundation of China (nos. 22174167, 11474364, 51573213, 51905557 and 51290271), and Key Laboratory of Sensing Technology and Biomedical Instruments of Guangdong Province (2020B1212060077). The work was also supported in part by the Australia-China Joint Institute for Health Technology and Innovation.

REFERENCES

(1) Kim, J.; Campbell, A. S.; de Ávila, B. E.-F.; Wang, J. Wearable Biosensors for Healthcare Monitoring. *Nat. Biotechnol.* **2019**, *37* (4), 389−406.

(2) Shih, B.; Shah, D.; Li, J. X.; Thuruthel, T. G.; Park, Y. L.; Iida, F.; Bao, Z. A.; Kramer-Bottiglio, R.; Tolley, M. T. Electronic Skins and Machine Learning for Intelligent Soft Robots. *Sci. Robot.* **2020**, *5* (41), No. eaaz9239.

(3) Fang, Y. S.; Zhao, X.; Tat, T.; Xiao, X.; Chen, G. R.; Xu, J.; Chen, J. All-In-One Conformal Epidermal Patch for Multimodal Biosensing. *Matter* **2021**, *4* (4), 1102−1105.

(4) Kim, J.; Lee, Y.; Kang, M.; Hu, L.; Zhao, S.; Ahn, J.-H. 2d Materials for Skin-Mountable Electronic Devices. *Adv. Mater.* **2021**, *33* (47), 2005858.

(5) You, I.; Mackanic, D. G.; Matsuhisa, N.; Kang, J.; Kwon, J.; Beker, L.; Mun, J.; Suh, W.; Kim, T. Y.; Tok, J. B. H.; Bao, Z. N.; Jeong, U. Artificial Multimodal Receptors Based on Ion Relaxation Dynamics. *Science* **2020**, *370* (6519), 961−965.

(6) Kim, D.-H.; Lu, N. S.; Ma, R.; Kim, Y.-S.; Kim, R.-H.; Wang, S. D.; Wu, J.; Won, S. M.; Tao, H.; Islam, A.; Yu, K. J.; Kim, T.-i.; Chowdhury, R.; Ying, M.; Xu, L. Z.; Li, M.; Chung, H.-J.; Keum, H.; McCormick, M.; Liu, P.; Zhang, Y.-W.; Omenetto, F. G.; Huang, Y. G.; Coleman, T.; Rogers, J. A. Epidermal Electronics. *Science* **2011**, *333* (6044), 838−843.

(7) Lee, S.; Franklin, S.; Hassani, F. A.; Yokota, T.; Nayeem, O. G.; Wang, Y.; Leib, R.; Cheng, G.; Franklin, D. W.; Someya, T. Nanomesh Pressure Sensor for Monitoring Finger Manipulation without Sensory Interference. *Science* **2020**, *370* (6519), 966−970.

(8) Jeong, H.; Lee, J. Y.; Lee, K.; Kang, Y. J.; Kim, J.-T.; Avila, R.; Tzavelis, A.; Kim, J.; Ryu, H.; Kwak, S. S.; Kim, J. U.; Banks, A.; Jang, H.; Chang, J.-K.; Li, S. P.; Mummidisetty, C. K.; Park, Y.; Nappi, S.; Chun, K. S.; Lee, Y. J.; Kwon, K.; Ni, X. Y.; Chung, H. U.; Luan, H. W.; Kim, J.-H.; Wu, C. S.; Xu, S.; Banks, A.; Jayaraman, A.; Huang, Y. G.; Rogers, J. A. Differential Cardiopulmonary Monitoring System for Artifact-Canceled Physiological Tracking of Athletes, Workers, and COVID-19 Patients. *Sci. Adv.* **2021**, *7* (20), No. eabg3092.

(9) Kwon, K.; Kim, J. U.; Deng, Y. J.; Krishnan, S. R.; Choi, J.; Jang, H.; Lee, K. H.; Su, C.-J.; Yoo, I.; Wu, Y. X.; Lipschultz, L.; Kim, J.-H.; Chung, T. S.; Wu, D. R.; Park, Y.; Kim, T. -i.; Ghaffari, R.; Lee, S.; Huang, Y. G.; Rogers, J. A. An on-Skin Platform for Wireless Monitoring of Flow Rate, Cumulative Loss and Temperature of Sweat in Real Time. *Nat. Electron.* **2021**, *4* (4), 302−312.

(10) Song, E. M.; Xie, Z. Q.; Bai, W. B.; Luan, H. W.; Ji, B. W.; Ning, X.; Xia, Y.; Baek, J. M.; Lee, Y. J.; Avila, R.; Chen, H.-Y.; Kim, J.-H.; Madhvapathy, S.; Yao, K. M.; Li, D. F.; Zhou, J. K.; Han, M. D.; Won, S. M.; Zhang, X. Y.; Myers, D. J.; Mei, Y. F.; Guo, X.; Xu, S.; Chang, J.-K.; Yu, X. G.; Huang, Y. G.; Rogers, J. A. Miniaturized Electromechanical Devices for the Characterization of the Biomechanics of Deep Tissue. *Nat. Biomed. Eng.* **2021**, *5* (7), 759−771.

(11) Ji, S. B.; Wan, C. J.; Wang, T.; Li, Q. S.; Chen, G.; Wang, J. W.; Liu, Z. Y.; Yang, H.; Liu, X. J.; Chen, X. D. Water-Resistant Conformal Hybrid Electrodes for Aquatic Endurable Electrocardiographic Monitoring. *Adv. Mater.* **2020**, *32* (26), 2001496.

(12) Son, D.; Kang, J.; Vardoulis, O.; Kim, Y.; Matsuhisa, N.; Oh, J. Y.; To, J. W. F.; Mun, J. W.; Katsumata, T.; Liu, Y. X.; McGuire, A. F.; Krason, M.; Molina-Lopez, F.; Ham, J.; Kraft, U.; Lee, Y.; Yun, Y.; Tok, J. B. H.; Bao, Z. N. An Integrated Self-Healable Electronic Skin

System Fabricated *via* Dynamic Reconstruction of a Nanostructured Conducting Network. *Nat. Nanotechnol.* **2018**, *13* (11), 1057−1065.
(13) Guo, R.; Sun, X. Y.; Yao, S. Y.; Duan, M. H.; Wang, H. Z.; Liu, J.; Deng, Z. S. Semi-Liquid-Metal-(Ni-EGaIn)-Based Ultraconformable Electronic Tattoo. *Adv. Mater. Technol.* **2019**, *4* (8), 1900183.
(14) Ershad, F.; Thukral, A.; Yue, J. P.; Comeaux, P.; Lu, Y. T.; Shim, H.; Sim, K.; Kim, N.-I.; Rao, Z. Y.; Guevara, R.; Contreras, L.; Pan, F. J.; Zhang, Y. C.; Guan, Y.-S.; Yang, P. Y.; Wang, X.; Wang, P.; Wu, X. Y.; Yu, C. J. Ultra-Conformal Drawn-on-Skin Electronics for Multifunctional Motion Artifact-Free Sensing and Point-of-Care Treatment. *Nat. Commun.* **2020**, *11* (1), 3823.
(15) Han, M. D.; Chen, L.; Aras, K.; Liang, C. M.; Chen, X. X.; Zhao, H. B.; Li, K.; Faye, N. R.; Sun, B. H.; Kim, J.-H.; Bai, W. B.; Yang, Q. S.; Ma, Y. H.; Lu, W.; Song, E. M.; Baek, J. M.; Lee, Y. J.; Liu, C.; Model, J. B.; Yang, G. J.; Ghaffari, R.; Huang, Y. G.; Efimov, I. R.; Rogers, J. A. Catheter-Integrated Soft Multilayer Electronic Arrays for Multiplexed Sensing and Actuation During Cardiac Surgery. *Nat. Biomed. Eng.* **2020**, *4* (10), 997−1009.
(16) Kang, J.; Tok, J. B. H.; Bao, Z. N. Self-Healing Soft Electronics. *Nat. Electron.* **2019**, *2* (4), 144−150.
(17) Ohm, Y.; Pan, C. F.; Ford, M. J.; Huang, X. N.; Liao, J. H.; Majidi, C. An Electrically Conductive Silver-Polyacrylamide-Alginate Hydrogel Composite for Soft Electronics. *Nat. Electron.* **2021**, *4* (3), 185−192.
(18) Tringides, C. M.; Vachicouras, N.; de Lázaro, I.; Wang, H.; Trouillet, A.; Seo, B. R.; Elosegui-Artola, A.; Fallegger, F.; Shin, Y.; Casiraghi, C.; Kostarelos, K.; Lacour, S. P.; Mooney, D. J. Viscoelastic Surface Electrode Arrays to Interface with Viscoelastic Tissues. *Nat. Nanotechnol.* **2021**, *16* (9), 1019−1029.
(19) Wang, C. Y.; Yokota, T.; Someya, T. Natural Biopolymer-Based Biocompatible Conductors for Stretchable Bioelectronics. *Chem. Rev.* **2021**, *121* (4), 2109−2146.
(20) Jeong, J.-W.; Yeo, W.-H.; Akhtar, A.; Norton, J. J. S.; Kwack, Y.-J.; Li, S.; Jung, S.-Y.; Su, Y. W.; Lee, W.; Xia, J.; Cheng, H. Y.; Huang, Y. G.; Choi, W.-S.; Bretl, T.; Rogers, J. A. Materials and Optimized Designs for Human-Machine Interfaces *via* Epidermal Electronics. *Adv. Mater.* **2013**, *25* (47), 6839−6846.
(21) Zhang, L.; Kumar, K. S.; He, H.; Cai, C. J. Y.; He, X.; Gao, H. X.; Yue, S. Z.; Li, C. S.; Seet, R. C.-S.; Ren, H. L.; Ouyang, J. Y. Fully Organic Compliant Dry Electrodes Self-Adhesive to Skin for Long-Term Motion-Robust Epidermal Biopotential Monitoring. *Nat. Commun.* **2020**, *11* (1), 4683.
(22) Pan, L.; Cai, P. Q.; Mei, L.; Cheng, Y.; Zeng, Y.; Wang, M.; Wang, T.; Jiang, Y.; Ji, B. H.; Li, D. C.; Chen, X. D. A Compliant Ionic Adhesive Electrode with Ultralow Bioelectronic Impedance. *Adv. Mater.* **2020**, *32* (38), 2003723.
(23) Xie, C. M.; Wang, X.; He, H.; Ding, Y. H.; Lu, X. Mussel-Inspired Hydrogels for Self-Adhesive Bioelectronics. *Adv. Funct. Mater.* **2020**, *30* (25), 1909954.
(24) Yang, J. C.; Mun, J.; Kwon, S. Y.; Park, S.; Bao, Z. N.; Park, S. Electronic Skin: Recent Progress and Future Prospects for Skin-Attachable Devices for Health Monitoring, Robotics, and Prosthetics. *Adv. Mater.* **2019**, *31* (48), 1904765.
(25) Zhao, Y.; Zhang, S.; Yu, T. H.; Zhang, Y.; Ye, G.; Cui, H.; He, C. Z.; Jiang, W. C.; Zhai, Y.; Lu, C. M.; Gu, X. D.; Liu, N. Ultra-Conformal Skin Electrodes with Synergistically Enhanced Conductivity for Long-Time and Low-Motion Artifact Epidermal Electrophysiology. *Nat. Commun.* **2021**, *12* (1), 4880.
(26) Sempionatto, J. R.; Lin, M. Y.; Yin, L.; De la Paz, E.; Pei, K.; Sonsa-ard, T.; Silva, A. N. D.; Khorshed, A. A.; Zhang, F. Y.; Tostado, N.; Xu, S.; Wang, J. S. An Epidermal Patch for the Simultaneous Monitoring of Haemodynamic and Metabolic Biomarkers. *Nat. Biomed. Eng.* **2021**, *5* (7), 737−748.
(27) Kwon, K.; Wang, H. L.; Lim, J.; Chun, K. S.; Jang, H.; Yoo, I.; Wu, D.; Chen, A. J.; Gu, C. G.; Lipschultz, L.; Kim, J. U.; Kim, J.; Jeong, H.; Luan, H. W.; Park, Y.; Su, C.-J.; Ishida, Y.; Madhvapathy, S. R.; Ikoma, A.; Kwak, J. W.; Yang, D. S.; Banks, A.; Xu, S.; Huang, Y. G.; Chang, J.-K.; Rogers, J. A. Wireless, Soft Electronics for Rapid, Multisensor Measurements of Hydration Levels in Healthy and Diseased Skin. *Proc. Natl. Acad. Sci. U.S.A.* **2021**, *118* (5), No. e2020398118.
(28) Choi, S.; Han, S. I.; Jung, D.; Hwang, H. J.; Lim, C.; Bae, S.; Park, O. K.; Tschabrunn, C. M.; Lee, M.; Bae, S. Y.; Yu, J. W.; Ryu, J. H.; Lee, S.-W.; Park, K.; Kang, P. M.; Lee, W. B.; Nezafat, R.; Hyeon, T.; Kim, D.-H. Highly Conductive, Stretchable and Biocompatible Ag-Au Core-Sheath Nanowire Composite for Wearable and Implantable Bioelectronics. *Nat. Nanotechnol.* **2018**, *13* (11), 1048−1056.
(29) Yeon, H.; Lee, H.; Kim, Y.; Lee, D.; Lee, Y.; Lee, J.-S.; Shin, J.; Choi, C.; Kang, J.-H.; Suh, J. M.; Kim, H.; Kum, H. S.; Lee, J.; Kim, D.; Ko, K.; Ma, B. S.; Lin, P.; Han, S.; Kim, S.; Bae, S.-H.; Kim, T.-S.; Park, M.-C.; Joo, Y.-C.; Kim, E.; Han, J.; Kim, J. Long-Term Reliable Physical Health Monitoring by Sweat Pore-Inspired Perforated Electronic Skins. *Sci. Adv.* **2021**, *7* (27), No. eabg8459.
(30) Ozer, E.; Kufel, J.; Myers, J.; Biggs, J.; Brown, G.; Rana, A.; Sou, A.; Ramsdale, C.; White, S. A Hardwired Machine Learning Processing Engine Fabricated with Submicron Metal-Oxide Thin-Film Transistors on a Flexible Substrate. *Nat. Electron.* **2020**, *3* (7), 419−425.
(31) Guimarães, C. F.; Gasperini, L.; Marques, A. P.; Reis, R. L. The Stiffness of Living Tissues and Its Implications for Tissue Engineering. *Nat. Rev. Mater.* **2020**, *5*, 351−370.
(32) Yang, Y. X.; Wei, X. F.; Zhang, N. N.; Zheng, J. J.; Chen, X.; Wen, Q.; Luo, X. X.; Lee, C.-Y.; Liu, X. H.; Zhang, X. C.; Chen, J.; Tao, C. Y.; Zhang, W.; Fan, X. A Non-Printed Integrated-Circuit Textile for Wireless Theranostics. *Nat. Commun.* **2021**, *12* (1), 4876.
(33) Lei, Z. Y.; Zhu, W. C.; Zhang, X. C.; Wang, X. J.; Wu, P. Y. Bio-Inspired Ionic Skin for Theranostics. *Adv. Funct. Mater.* **2021**, *31* (8), 2008020.
(34) Tan, P.; Wang, H. F.; Xiao, F. R.; Lu, X.; Shang, W. H.; Deng, X. B.; Song, H. F.; Xu, Z. Y.; Cao, J. F.; Gan, T. S.; Wang, B.; Zhou, X. C. Solution-Processable, Soft, Self-Adhesive, and Conductive Polymer Composites for Soft Electronics. *Nat. Commun.* **2022**, *13* (1), 358.
(35) Tian, L. M.; Zimmerman, B.; Akhtar, A.; Yu, K. J.; Moore, M.; Wu, J.; Larsen, R. J.; Lee, J. W.; Li, J. H.; Liu, Y. H.; Metzger, B.; Qu, S. B.; Guo, X. G.; Mathewson, K. E.; Fan, J. A.; Cornman, J.; Fatina, M.; Xie, Z. Q.; Mao, Y. J.; Zhang, J.; Zhang, Y. H.; Dolcos, F.; Fabiani, M.; Gratton, G.; Bretl, T.; Hargrove, L. J.; Braun, P. V.; Huang, Y. G.; Rogers, J. A. Large-Area MRI-Compatible Epidermal Electronic Interfaces for Prosthetic Control and Cognitive Monitoring. *Nat. Biomed. Eng.* **2019**, *3* (3), 194−205.
(36) Cai, P. Q.; Wan, C. J.; Pan, L.; Matsuhisa, N.; He, K.; Cui, Z. Q.; Zhang, W.; Li, C. C.; Wang, J. W.; Yu, J.; Wang, M.; Jiang, Y.; Chen, G.; Chen, X. D. Locally Coupled Electromechanical Interfaces Based on Cytoadhesion-Inspired Hybrids to Identify Muscular Excitation-Contraction Signatures. *Nat. Commun.* **2020**, *11*, 2183.
(37) Ye, G.; Qiu, J. K.; Fang, X. Y.; Yu, T. H.; Xie, Y. Y.; Zhao, Y.; Yan, D. P.; He, C. Z.; Liu, N. A Lamellibranchia-Inspired Epidermal Electrode for Electrophysiology. *Mater. Horiz.* **2021**, *8*, 1047−1057.

https://doi.org/10.1021/acsnano.2c03414
ACS Nano XXXX, XXX, XXX−XXX